Atmospheric
Chemistry
and Physics

Age spectra and other transport diagnostics in the North American monsoon UTLS from SEAC4RS in situ trace gas measurements

Eric A. Ray[1,2]**, Elliot L. Atlas**[3]**, Sue Schauffler**[4]**, Sofia Chelpon**[5]**, Laura Pan**[4]**, Harald Bönisch**[6]**, and Karen H. Rosenlof**[1]

[1]NOAA Chemical Sciences Laboratory, Boulder, CO, USA
[2]Cooperative Institute for Research in Environmental Science (CIRES),
University of Colorado, Boulder, CO, USA
[3]University of Miami, Miami, FL, USA
[4]National Center for Atmospheric Research, Boulder, CO, USA
[5]City University of New York Graduate Center, New York, NY, USA
[6]Karlsruhe Institute of Technology, Institute of Meteorology and Climate Research, Karlsruhe, Germany

Correspondence: Eric A. Ray (eric.ray@noaa.gov)

Abstract. The upper troposphere and lower stratosphere (UTLS) region during the summer monsoon season over North America (NAM) is influenced by the transport of air from a variety of source regions over a wide range of timescales (hours to years). Age spectra are useful for characterizing the transport into such a region, and in this study we use and build on recently developed techniques to infer age spectra from trace gas measurements with photochemical lifetimes from days to centuries. We show that the measurements taken by the whole-air sampler instrument during the SEAC4RS campaign can be used to derive not only age spectra, but also path-integrated lifetimes of each of the trace gases and partitioning between North American and tropical surface source origins. The method used here can also clearly identify and adjust for measurement outliers that were influenced by polluted surface source regions. The results are generally consistent with expected transport features of the NAM but also provide a range of transport diagnostics (age spectra, trace gas lifetimes and surface source regions) that have not previously been computed solely from in situ measurements. These methods may be applied to many other existing in situ datasets, and the transport diagnostics can be compared with chemistry–climate model transport in the UTLS.

1 Introduction

The upper troposphere and lower stratosphere (UTLS) area in the region of the North American monsoon (NAM) is influenced by rapid transport from convection that penetrates from below, mixing due to wave breaking and transport in the lower branch of the Brewer–Dobson circulation, as well as slowly descending air from the stratosphere above (Weinstock et al., 2007; Boenisch et al., 2009; Orbe et al., 2015; von Hobe et al., 2021). The timescales of these different transport pathways from the surface to the UTLS range from

hours to years, and thus this part of the atmosphere, especially over the monsoon regions during summer, contains a uniquely complex dynamical history and chemical composition. A number of previous studies have used in situ trace gas measurements to estimate average transport characteristics of the summer UTLS such as the tropospheric fraction (Ray et al., 1999; Weinstock et al., 2007) and mean age of air (Boenisch et al., 2009; Birner et al., 2020). However, average transport quantities do not fully capture the complexity of the region, so more sophisticated transport descriptions, such as age spectra and surface source region identification,

have also been estimated primarily from model simulations (Diallo et al., 2012; Orbe et al., 2015; Ploeger and Birner, 2016; Hauck et al., 2019). The modeled transport quantities provide useful information but are also dependent on a variety of input meteorological products that can produce different results (Ploeger et al., 2019).

Most previous studies of the age of air from trace gas measurements have focused on the stratosphere and used species with very long lifetimes that increase in time, such as CO_2 and SF_6 (e.g., Andrews et al., 1999, 2001; Waugh and Hall, 2002). For these trace gases the age of air can be inferred from mixing ratio differences between measurement locations and a source region, typically the tropical tropopause since this is where most of the air enters the stratospheric overworld. Trace gases with significant local photochemical loss along pathways from the source region to the measurement locations can also be used to calculate the age of air, but in this case the path-integrated lifetimes need to be estimated to account for the photochemical loss. The path-integrated lifetime is different from the local photochemical lifetimes and is unique to each measurement time, location and trace gas. This is complementary to the age of air since it reveals pathway information through known local photochemical loss regions (e.g., Hall, 2000; Moore et al., 2014). Although the path-integrated lifetime is essentially a by-product of the age spectra calculation, it can be utilized as a transport diagnostic in its own right since it could be used to help explain differences between observed and modeled trace gases in the UTLS. Schoeberl et al. (2005) were the first to estimate stratospheric age spectra using multiple trace gases with relatively short local stratospheric lifetimes, such as N_2O and CFC-11, and to solve for the path-integrated lifetime of each trace gas at individual locations.

The UTLS presents more challenges to calculate the age of air, path-integrated lifetimes and other transport diagnostics due to the wide range of possible source regions and relatively rapid transport and mixing compared to the stratospheric overworld. Recent studies have taken advantage of the predominance of emissions of anthropogenically produced trace gases in the Northern Hemisphere (NH) compared to the Southern Hemisphere (SH) to calculate inter-hemispheric transport diagnostics in the troposphere based on the differences in NH–SH surface trace gas measurements (Waugh et al., 2013; Holzer and Waugh, 2015). The inter-hemispheric transport timescale is on the order of a year, but more generally calculating transport diagnostics at any location in the free troposphere from the surface requires resolving transport timescales of hours in the case of convective transport. This rapid transport can only be clearly detected in very short-lived trace gases (path-integrated lifetimes of days). Luo et al. (2018) used in situ trace gas measurements over the tropical Pacific Ocean with a range of lifetimes from days to centuries to derive the transit time distribution from the surface to the tropical upper troposphere. The terminology "transit time distribution" is commonly used in studies focused on the troposphere and is equivalent in meaning to the "age spectrum" typically used in stratospheric studies. The Luo et al. (2018) study was one of the first to bring stratospheric age of air techniques to tropospheric measurements and was unique in the use of such a wide range of trace gases with different lifetimes.

In the UTLS, age spectra derived from trace gas measurements have been somewhat rare (Ehhalt et al., 2007; Boenisch et al., 2009), although recent studies have developed new techniques with promising results (Luo et al., 2018; Hauck et al., 2019, 2020; Podglajen and Ploeger, 2019). The studies of Hauck et al. (2019, 2020) focused on the lowermost stratosphere and an inverse technique following Schoeberl et al. (2005) with the tropopause as the source region. These studies introduce an imposed seasonal cycle on the age spectra based on model output as well as tropical and extratropical source regions following the known transport pathways to the lowermost stratosphere (e.g., Ray et al., 1999; Boenisch et al., 2009). The partitioning between the tropical and extratropical source regions is also prescribed based on model output. These studies are essentially a hybrid of theoretical, observational and model analysis. The path-integrated lifetimes of the trace gases are estimated in Hauck et al. (2020) along with the age spectra, but the lifetimes are not shown.

As a starting point for this work, we use the technique put forth in Luo et al. (2018). In addition to the use of a wide range of trace gases, this study also introduced the novel path-integrated lifetime vs. normalized mixing ratio framework, which we use extensively. In the current study we use measurements taken during the Studies of Emissions and Atmospheric Composition, Clouds and Climate Coupling by Regional Surveys (SEAC[4]RS) mission in the UTLS over North America during the NAM, primarily from the whole-air sampler (WAS) instrument on the ER-2 aircraft. The fundamental differences in the calculation presented here compared to Luo et al. (2018) and to other previous studies are that, in addition to finding age spectra, we solve for surface source regions of air from the tropics and NH extratropics, and we find path-integrated lifetimes for each trace gas for the sampled UTLS. We use a combination of measurements of 20 trace gases with a variety of photochemical lifetimes as well as CO_2, which together provide powerful constraints on the derived transport quantities.

We describe the data used in this work in Sect. 2 and the general method in Sect. 3. Results for the average theta profiles over the whole SEAC[4]RS mission and for individual measurement locations are shown in Sect. 4. The calculation performed here has many details and assumptions, some of which are described more fully in the Supplement.
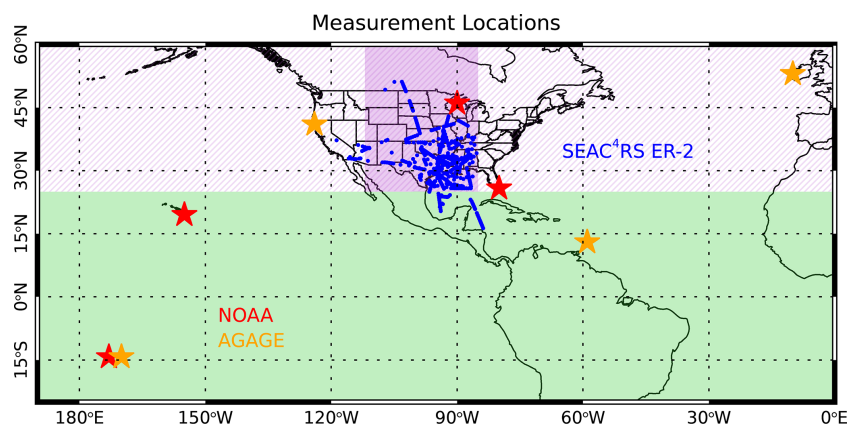
Figure 1. Map of the location of SEAC[4]RS ER-2 in situ measurements in the UTLS (blue symbols) and surface NOAA (red) and AGAGE (orange) measurement stations used in the analysis. The darker shaded purple region is where CarbonTracker NAM ($1° \times 1°$ resolution) data were used to calculate NA CO_2 surface time series, and the light green shaded region indicates where CarbonTracker Global ($3° \times 2°$ resolution) was used. For the other trace gases used in the analysis either individual surface stations (stars) or zonal means (light purple and green shaded regions) were used to calculate the tropical and NA time series (see Table 1).

2 Data

The UTLS data used in this study were taken during the SEAC[4]RS mission, which took place in August and September 2013 over North America (Toon et al., 2016). We used measurements of 20 different species from the whole-air sampler (WAS) instrument on the ER-2 (Table 1) as well as CO_2 measurements from the Harvard Picarro cavity ring-down spectrometer (PCRS), O_3 from the NOAA unmanned aircraft system (UAS) O_3 instrument, and water vapor from the JPL laser hygrometer (JLH). The 20 species measured by WAS were chosen due to their range of lifetimes and lack of significant production in the atmosphere. We used the WAS merge data files (https://www-air.larc.nasa.gov/cgi-bin/ArcView/seac4rs?MERGE=1#WAS.ER2_MRG/, last access: 1 June 2019), which put all of the trace gas and meteorological measurements on the WAS sampling frequency of ~ 4–5 min. In total we used data from the 548 WAS sampling times during the mission above the 340 K potential temperature surface, although not all of the trace gases are available at all of the sampling times.

Surface measurements come from the NOAA Global Monitoring Laboratory (GML) network for 16 of the 20 trace gases and from the Advanced Global Atmospheric Gases Experiment (AGAGE) network for three of the trace gases. 1,2-Dichloroethane is not regularly measured by either network, so we used a constant mixing ratio in each latitude region based on previously published measurements (Class and Ballschmiter, 1987). CO_2 boundary layer mixing ratios were obtained from NOAA's CarbonTracker version CT2019B (Jacobsen et al., 2020) (see Sect. S1 in the Supplement for details).

This calculation requires time series of each trace gas in a range of latitudes that span the expected source regions of

air to the NH UTLS (Ray et al., 2004; Herman et al., 2017), roughly from the Equator to the high northern latitudes. We extend the surface time series back 30 years prior to the time of the SEAC[4]RS mission. To construct each trace gas time series, we used surface network measurements when available (Table 1), and when measurements were not available, we extended the time series backward to the year 1983 based on published trends and calculated seasonal cycles. For the shortest-lived trace gases, such as propane, only the previous several months are important for deriving the surface boundary conditions, so the seasonal cycle is sufficient to create the surface time series. For the longest-lived trace gases, such as the CFCs and HCFCs, we extrapolated backward from the earliest available measurements using the growth rate over the 2 subsequent years. Examples of these surface time series for ethane are shown in Fig. 2. Both the seasonal cycle and latitudinal gradient are substantial for ethane and many other trace gases used in this study, so the boundary layer (BL) mixing ratios are sensitive to the surface source region as well as the age spectra.

The calculation of transport diagnostics also requires an estimate of the lifetime of each trace gas as shown in Table 1. The lifetimes in the calculation are path-integrated lifetimes from the surface source regions. There can be many pathways to a location in the UTLS, so exact lifetimes are not known. The values shown in Table 1 are initial estimates of the path-integrated lifetimes of each trace gas in the sampled upper troposphere, specifically in the 350–360 K layer, based on local lifetime estimates in the troposphere and lower stratosphere. The sources of local lifetime estimates are listed in Table 1, with the primary sources of tropospheric lifetimes from Luo et al. (2018) and Chelpon et al. (2021) and the primary source of stratospheric lifetimes from the WMO (2018). Since the 350–360 K layer sampled

Table 1. List of trace gases used in this study, their estimated upper tropospheric lifetimes and the sources of the surface time series.

Trace gas	Initial UT lifetime (days)[1]	Surface data source	30-year extension source
n-Butane, C_4H_{10}	8	NOAA GML stations[2]	Seasonal cycle
Isobutane, C_4H_{10}	9	NOAA GML stations	Seasonal cycle
Propane, C_3H_8	14	NOAA GML zm[3]	Seasonal cycle
Ethyne, C_2H_2	16	NOAA GML zm	Seasonal cycle
1,2-Dichloroethane, $C_2H_4Cl_2$	30	Constant[4]	Constant
Ethane, C_2H_6	80	NOAA GML zm	Trend[6]
Perchloroethylene, C_2Cl_4	100	AGAGE stations[5]	Measured GR[7]
Chloroform, $CHCl_3$	200	AGAGE stations	Measured GR
HFC-152a, $C_2H_4F_2$	600	NOAA GML zm	Measured GR
Methyl bromide, CH_3Cl	800	NOAA GML zm	Measured GR
HCFC-141b, CH_3CCl_2F	3000	NOAA GML zm	Measured GR
HCFC-22, $CHClF_2$	4000	NOAA GML zm	Measured GR
HFC-134a, CH_2FCF_2	5000	NOAA GML zm	Measured GR
Halon-1211, $CBrClF_2$	6000	NOAA GML zm	Measured GR
HCFC-142b, CH_3CClF_2	7000	NOAA GML zm	Measured GR
Carbon tetrachloride, CCl_4	10 000	NOAA GML zm	Measured GR
CFC-11, CCl_3F	15 000	NOAA GML zm	Measured
CFC-113, $C_2Cl_3F_3$	20 000	NOAA GML zm	Measured GR
CFC-12, CCl_2F_2	25 000	NOAA GML zm	Measured
CFC-114, $C_2Cl_2F_4$	60 000	AGAGE stations	Measured GR

[1] UT lifetimes refer to path-integrated lifetimes based on tropospheric and lower stratospheric local lifetimes of each trace gas from WMO (2018), Luo et al. (2018), Chelpon et al. (2021), Tang et al. (2007), Hodnebrog et al. (2018), Wuebbles et al. (2007), Olaguer (2002), Chipperfield et al. (2013) and Singh et al. (1996). [2] NOAA GML stations used were Samoa, Mauna Loa, Key Biscayne and Wisconsin (LEF). [3] NOAA GML zonal mean surface time series are calculated in seven different latitude bands from all available flask and in situ measurement sites. (https://www.esrl.noaa.gov/gmd/hats/data.html, last access: 1 June 2019) (G. Dutton, personal communication, 2020). [4] The 1,2-dichloroethane time series is a constant in each latitude bin with latitude gradients based on the measurements of Class and Ballschmiter (1987). [5] AGAGE stations used were Samoa, Ragged Point Barbados, Trinidad Head and Mace Head. [6] Ethane growth rate from Helmig et al. (2016). [7] Measured GR refers to the use of the growth rate based on the earliest available 2 years of measurements applied to extend the time series back to 1983.

during SEAC4RS was in the subtropical upper troposphere, the path-integrated lifetimes shown in Table 1 are weighted towards UT local lifetimes as in Chelpon et al. (2021). These lifetimes are used as initial estimates in the calculation but are adjusted for each theta layer and each individual measurement location based on the best-fit age spectra as described below. Thus, while it is important to have the initial path-integrated lifetime estimates for the calculation, the final derived lifetimes are considerably different from those shown in Table 1.

CO_2 is used as an additional constraint on the age spectra calculated from the 20 trace gases listed in Table 1, and thus 30-year surface time series over a range of latitudes are also necessary to convolve with the age spectra. Carbon-Tracker contains both a global gridded CO_2 product and a higher-resolution gridded product over North America. For surface latitudes in the region sampled by SEAC4RS (20–50° N) (Figs. 1, S2) we use the North American (NA) product zonally averaged from 85–112° W, and for tropical latitudes we use full zonal means of the global product. The reason for this different range of surface longitudes is that it is assumed that the influence from tropical latitudes will

have traveled some distance and be relatively well mixed in longitude compared to the local convective influence in the sampled NA region.

For some of the trace gases a scaling was applied to account for calibration offsets between WAS measurements and those from the surface networks. These scaling values were estimated based on the best agreement with DC-8 WAS measurements near the surface during SEAC4RS as well as expected relationships between normalized trace gases in the upper troposphere from previously calculated tropospheric lifetimes. The specific scaling values and methodology are provided in Sect. S1. It should be noted that the scaling does not significantly affect the age spectra calculation and that the scaling factors are on the order of 1 %–5 %.

3 Methods

The mixing ratio of a trace gas, i, at a particular location x and time t in the atmosphere can be expressed as

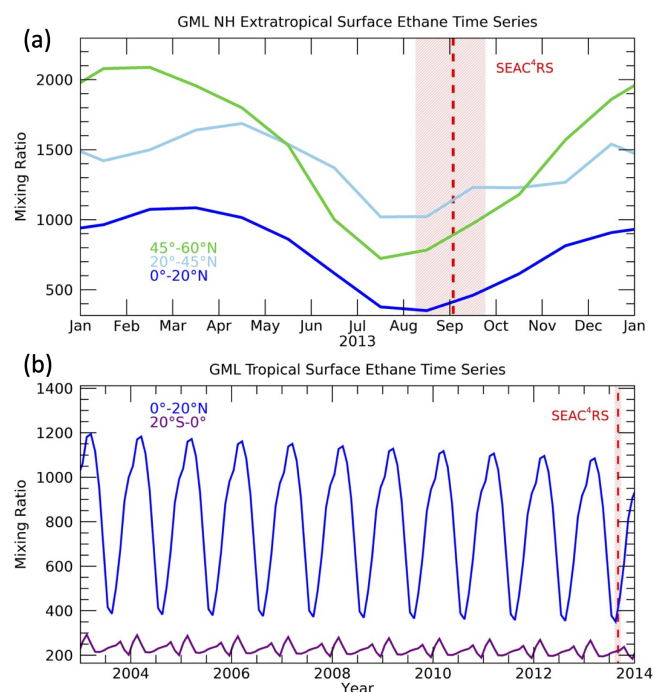$$\chi_i(x,t) = \int_0^\infty \chi_{io}(t - t') e^{-t'/\tau_i(x,t')} G(x,t,t') \, dt', \quad (1)$$

Figure 2. Time series of ethane at the surface in **(a)** NH extratropical and **(b)** tropical latitude bands. The timing of the SEAC^{4}RS mission is indicated by the red shading covering all of the flights, and the dashed red line indicates the mission average date.

where t' is the transit time or age from a source region, τ_i is the path-integrated lifetime of the trace gas, $\chi_{io}(t-t')$ is the mixing ratio time series at the source region and G is the age spectrum of all the paths from the source region to the location x (e.g., Schoeberl et al., 2000; Ehhalt et al., 2007; Hauck et al., 2019). The age spectra can be assumed to have a functional form following many previous studies of the age of air in the stratosphere (e.g., Hall and Plumb, 1994; Schoeberl et al., 2005):

$$G\left(K, z, t'\right) = \frac{z}{2\sqrt{\pi K t'^3}} \exp\left(\frac{z}{2H} - \frac{K t'}{4H^2} - \frac{z}{4K t'}\right), \quad (2)$$

where H is the scale height, z is the altitude and K is an effective diffusion coefficient that varies with location. We have removed a dependence of G on t since this study only considers measurements over a period of roughly 1 month. This functional form allows the age spectra to be defined by a single parameter K at a particular altitude z. Thus, in the rest of the paper we refer to the age spectra with dependence on K, z and t'.

In Luo et al. (2018) and Chelpon et al. (2021) it was shown that there is a compact relationship between measured trace gas mixing ratios in the tropical upper troposphere (UT) normalized by local marine boundary layer (BL) mixing ratios, referred to as the measured UT fraction (μ^*), vs. lifetime (τ) over a wide range of trace gases. A similar compact relationship was originally found by Ehhalt et al. (2007). The Luo

et al. (2018) and Chelpon et al. (2021) studies made the approximations of steady-state and 1D conditions in order to rearrange Eq. (1) to solve for an idealized form of μ:

$$\mu_i(K, z) = \frac{\chi_i(z)}{\chi_{io}} = \int_0^\infty e^{-t'/\tau_i} G\left(K, z, t'\right) dt', \quad (3)$$

where χ_{io} is a constant BL mixing ratio of trace gas i and $\chi_i(z)$ is an idealized UT mixing ratio of trace gas i at height z. With this formulation, each age spectra G produces a unique idealized $\mu(\tau)$ curve that can be compared to the measurement-based $\mu^*(\tau)$ values. The age spectrum that produces the $\mu(\tau)$ curve with the best fit to the $\mu^*(\tau)$ values is assumed to be the best approximation of the age spectrum at the measurement location and time.

The general philosophy of the method used here is to maximize the information available in the wide range of trace gas measurements both in the UTLS and at the surface. Figure 3 summarizes the main transport features in this region and our conceptual framework of dividing the surface into two broad latitudinal regions, the tropics and NA. We utilize the $\mu(\tau)$ and $\mu^*(\tau)$ relationships to identify transport parameters that best fit the measurements and describe how air moves from the surface to the UTLS in the NAM region in more detail than has been done previously. Guided by this framework and the strength of the high-quality, simultaneous trace gas measurements, we can drill down to reveal unique details of latitudinal source regions, path-dependent lifetimes and fractions of air from each surface region, among others. In the rest of this section, we go into detail on how these transport parameters were formulated and the assumptions we have chosen to make.

We consider the latitudinal dependence of χ_{io}, which means we need to construct BL time series for all of the trace gases at a range of latitudes as described in the previous section, but also the fact that the normalized mixing ratios μ and μ^*, which we will refer to as BL fractions, will have latitudinal source region and age dependencies. The primary BL source latitudes to the sampled UTLS (Figs. 1 and 3) are not known a priori so this is a free parameter in the calculation. Based on many previous studies of UTLS transport (e.g., Orbe et al., 2013, 2015), we can apply some general constraints to the possible BL source latitudes and allow the calculation to optimize among them. The UTLS up to 400 K was shown in previous studies to have been significantly influenced by convective transport from the North American continent during the SEAC^{4}RS mission (e.g., Herman et al., 2017). Convective transport from the BL can occur on the timescale of hours and if it enters the stratosphere can remain there for days to months depending on the depth above the tropopause. The onset of NAM convection each year generally occurs in early June (e.g., Clapp et al., 2020), roughly 2 to 3 months before the August–September time frame of the SEAC^{4}RS mission. Thus, the oldest air that

would have been convectively transported from the local, extratropical surface to the sampled UTLS would likely be 2 to 3 months. This would represent air that was convectively injected in June or July into the lowermost stratosphere where it then slowly descended to the sampled location by August or September. There could also be air from the NA surface more than 3 months old in the LS that was not convectively injected, but rather took a longer path via the tropical UT where it could then have been isentropically transported into the LS. The Asian summer monsoon is also known to be a significant source of air to the extratropical UTLS (e.g., Yu et al., 2017). Since we do not have sufficient surface measurement time series in the Asian monsoon region, we cannot include Asia as a separate extratropical source region in this study.

Air from the tropical surface can be transported to the extratropical UTLS initially by convection to the tropical transition layer and then either by isentropic transport or through the stratosphere by the Brewer–Dobson circulation (e.g., Boenisch et al., 2009). The transport times for these pathways from the tropical surface range from days to decades (e.g., Ploeger et al., 2019) (Fig. 3).

Based on these transport characteristics of air from the surface to the extratropical UTLS we partition the age spectra into transport from tropical and NA surface source regions as shown schematically in Fig. 3. We follow the ansatz of Hauck et al. (2020), although we neglect the transport from the SH and use the surface as our source region as opposed to the tropopause in that study. The partitioning of the age spectra can be expressed as

$$G\left(K, z, t'\right) = g_{\text{TR}}\left(K, z, t'\right) + g_{\text{NA}}\left(K, z, t'\right), \tag{4}$$

where g_{TR} and g_{NA} are the age spectra from tropical (25° S–25° N) and NA surface latitudes (25–55° N), respectively, and the lowercase g indicates age spectra that are nonnormalized. The fraction of air from each region that contributed to the sampled UTLS can be calculated by the integration of the age spectra:

$$\int_0^\infty G\left(K, z, t'\right) dt' = \int_0^\infty g_{\text{TR}}\left(K, z, t'\right) dt' + \int_0^\infty g_{\text{NA}}$$
$$\left(K, z, t'\right) dt' = F_{\text{TR}}\left(K, z\right) + F_{\text{NA}}\left(K, z\right) = 1, \tag{5}$$

where F_{TR} and F_{NA} refer to the fractions of air from the NA and tropical surface, respectively.

Up to this point all of the equations follow from general theory established in previous studies (e.g., Holzer and Hall, 2000; Ehhalt et al., 2007; Luo et al., 2018; Hauck et al., 2020) and provide the framework for the calculations performed here. The main assumptions thus far are the parameterized form of the age spectra (Eq. 2) and the choice of two main source regions each with their own age spectra (Eq. 4). In the rest of this section, we describe several additional approximations and assumptions that are unique to this study and

allow us to calculate the individual source region age spectra g_{TR} and g_{NA} and the most likely surface source latitudes in each region.

To calculate g_{TR} and g_{NA} we assume that the shortest timescales (hours to weeks) of the whole age spectra G are primarily from NA latitudes and that longer timescales (weeks to years) are primarily from tropical surface latitudes (Figs. 1 and 3). Transport timescales on the order of months can have significant contributions from both NA and tropical latitudes. Based on this assumption, g_{TR} and g_{NA} can be expressed as scaled functions of G.

$$g_{\text{TR}}\left(K, z, t'\right) = f(z, t')G\left(K, z, t'\right) \tag{6}$$
$$g_{\text{NA}}\left(K, z, t'\right) = (1 - f(z, t'))G\left(K, z, t'\right) \tag{7}$$

The scaling factor f has an age dependence with a Gaussian form such that $f(0) = 0$ and $f(t'_{\text{f}}) = 1$ (Fig. S3). Thus, at $t'_{\text{f}}/2$ the total age spectrum is evenly divided between tropical and NA surface source regions. The scaling factor is not known a priori so we ran the calculation with values of t'_{f} from 30 to 200 d and found the optimum values at each theta level (see Sect. S2), which is why f has a z dependence in Eqs. (4) and (5). The values of t'_{f} we use range from 50 d below 380 K to 150 d above 400 K.

A unique aspect of this approach is that while we have specified the total age spectra G to have the commonly used inverse Gaussian shape as shown by Eq. (2), the individual region age spectra g_{TR} and g_{NA} are not constrained in this way and so will have different shapes. The individual region age spectra are still constrained overall by the shape of G and the form of the scaling factor f, so there is a limit to the possible shapes of g_{TR} and g_{NA}. As will be shown below, we allow the calculation to optimize among a wide range of possible total age spectra G (see Sect. S4). The mean ages of the possible G vary from several months to several years, and modal ages are as young as 1 d. The tails of the age spectra G are extended to 30 years, so that is the upper limit used in the time integrations.

We now have a method to calculate separate source region age spectra from the total age spectra G, but referring back to Eqs. (1) and (3), we note that to obtain $\mu^*(\tau)$ values for each set of measurements and to solve for the G that provides the best fit, we need χ_i time series from all source latitudes to calculate values of χ_{io}. Thus, the true start of the method is to find the values of χ_{io}. The most straightforward approach to calculate χ_{io} is to average $\chi_i(y_o, t')$ over all of the surface latitudes (y_o) that we consider to find a single surface time series for each trace gas, $\overline{\chi}_{io}(t')$. This approach assumes all of the surface latitudes contribute equally as source regions to the NAM UTLS. But since we know that there are preferential convective regions in NA, such as the US Midwest, and in the tropics, such as the Intertropical Convergence Zone (ITCZ), it makes more sense to average over a number of different latitude bands within each region and allow the op-
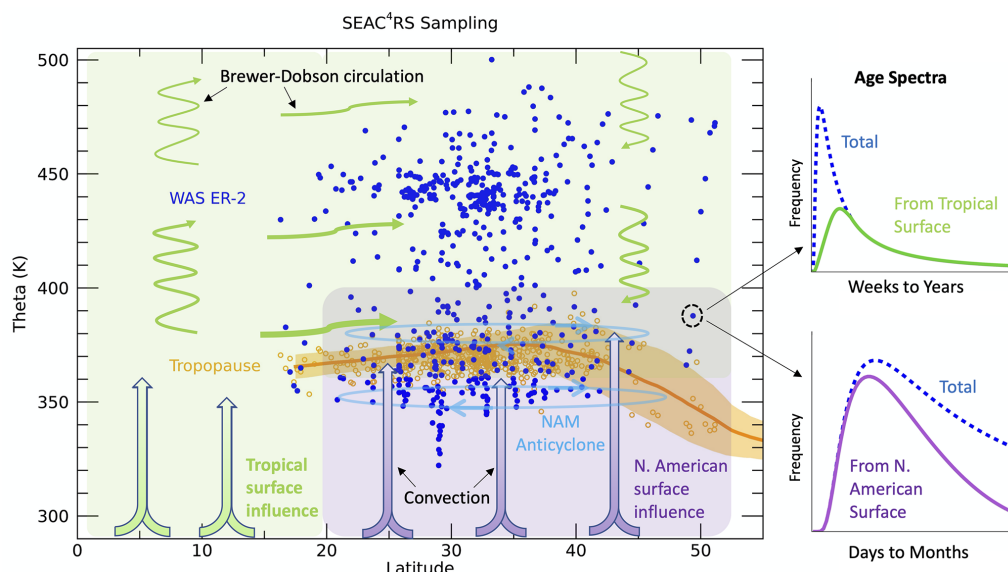
Figure 3. Sampling of the WAS measurements on the ER-2 (blue symbols) during SEAC[4]RS as well as indicators of the tropopause levels based on microwave temperature profiler (MTP) measurements (orange symbols) and from MERRA2 averaged over the mission time period and sampling area (average as an orange line and standard deviation in orange shading). The purple shading and thick arrows indicate convective transport from the North American surface to the UTLS, while the green arrows and shading indicate transport from the tropical surface to the sampled UTLS through convection followed by isentropic mixing and/or advection by the Brewer–Dobson circulation. The NAM anticyclone circulation is indicated by the light blue ovals. Age spectra examples for an individual measurement location are shown on the right. The total spectrum is shown by the blue dashed lines in each plot and the partitioning of the spectrum into that from the tropical surface (light green, top) for longer timescales and from the North American surface (purple, bottom) for shorter timescales.

timization to identify the primary source latitudes in each region at the same time we find the best-fit G.

The initial step in the calculation of χ_{io} is to divide the surface source latitudes into the same two regions as was done for the age spectra. We then subdivide each region into latitude bands by averaging the surface time series over Gaussian distributions (L_{TR}, L_{NA}) with peaks separated by 4° latitude and half-widths of 10° (Fig. S4). These averaged surface time series are calculated by

$$\chi_{iTR}\left(t', y_{pTR}\right) = \int_{y_1}^{y_2} \chi_i\left(y_o, t'\right) L_{TR}\left(y_o, y_{pTR}\right) dy_o, \quad (8)$$

$$\chi_{iNA}\left(t', y_{pNA}\right) = \int_{y_1}^{y_2} \chi_i\left(y_o, t'\right) L_{NA}\left(y_o, y_{pNA}\right) dy_o, \quad (9)$$

where y_o is the surface latitude, $y_1 = 20°$ S, $y_2 = 70°$ N, and y_{pTR} and y_{pNA} represent the peak surface latitudes of the distributions in the tropics and NA, respectively. These averaged surface trace gas time series representing the subregions within the tropics and NA are then convolved in time with the

age spectra from each region by

$$\chi_{ioTR}\left(K, z, y_{pTR}\right) = \int_0^\infty \chi_{iTR}\left(t', y_{pTR}\right) g_{TR}\left(K, z, t'\right) dt',$$
$$(10)$$

$$\chi_{ioNA}\left(K, z, y_{pNA}\right) = \int_0^\infty \chi_{iNA}\left(t', y_{pNA}\right) g_{NA}\left(K, z, t'\right) dt'. \quad (11)$$

Note that χ_{ioTR} and χ_{ioNA} are scaled BL mixing ratios since the age spectra from each region, g_{TR} and g_{NA}, are scaled by the fraction of air from each region F_{TR} and F_{NA}. The actual BL mixing ratios from each region can be found by χ_{ioTR}/F_{TR} and χ_{ioNA}/F_{NA}. The total BL trace gas mixing ratios are then given by

$$\chi_{io}\left(K, z, y_{pTR}, y_{pNA}\right) = \chi_{ioTR}\left(K, z, y_{pTR}\right) + \chi_{ioNA}\left(K, z, y_{pNA}\right). \quad (12)$$

The values of χ_{io} represent a large range of possible source mixing ratios to the NAM UTLS from the tropical and NA surface with transport times parameterized by K. This set of BL mixing ratios is calculated for each parameter combination and all trace gases as the initial step of the method. The values of χ_{io} are only calculated once and then used to find the range of possible BL fractions for every set of measure-

ments by

$$\mu_i^* \left(K, z, y_{\text{pTR}}, y_{\text{pNA}} \right) = \frac{\chi_i^*(z,t)}{\chi_{io} \left(K, z, y_{\text{pTR}}, y_{\text{pNA}} \right)}, \quad (13)$$

where $\chi_i^*(z,t)$ is the measured mixing ratio of trace gas i at altitude z and time t. The measurement-based μ_i^* values can then be compared to the idealized μ_i values (Eq. 3). We also calculated CO_2 BL mixing ratios ($\chi_{CO_2o}^*$) with the same set of equations (Eqs. 8–12) as for the other trace gases. Since the lifetime of CO_2 is essentially infinite in the context of this study, rather than normalizing the measured CO_2 mixing ratios ($\chi_{CO_2o}^*$) we simply compare them to the range of possible values of $\chi_{CO_2o}^*$ based on the set of transport parameters. Thus, we utilize CO_2 as an additional constraint to find the best set of parameters that describe the transport to the measurement locations.

We perform the calculation initially with theta average trace gas profiles beginning with the lowest layer of 350–360 K and work up to the highest layer of 470–480 K. We begin with theta average profiles since they provide a robust, smoothly varying set of measurements to establish the validity of the calculation. And we begin with the lowest theta layer since we have a reasonable initial estimate of the path-dependent lifetimes τ_i in the UT as shown in Table 1. With the results from the theta average profiles (Sect. 4) as a starting point, we can then perform the calculation on the highly variable individual location measurements (Sect. 5).

The main steps of the method can be summarized as follows.

1. Calculate BL mixing ratios (χ_{io}) of all trace gases including CO_2.

2. Calculate BL fractions (μ_i^*) for the lowest theta average layer.

3. Use UT path-dependent lifetimes τ_i as shown in Table 1.

4. Identify optimal transport parameters ($K, y_{\text{pTR}}, y_{\text{pNA}}$) based on combined minimum differences between μ_i^* and μ_i and between $\chi_{CO_2}^*$ and $\chi_{CO_2o}^*$.

5. Adjust τ_i values to match the best-fit idealized $\mu(\tau)$ relationship.

6. Repeat steps 2–5 for the next higher theta layer with τ_i values initialized from layer below.

There are a number of details to each step of the method, which are described in Sect. S4. The method for the individual location measurements is similar to step 6, but the τ_i values are initialized with the values from the theta layer average result that encompasses the location of the individual measurement. The theta layer optimized value of K is also used as a starting point for the individual measurements since this helps identify outliers due to polluted source regions, as will be described in Sect. 5.

As examples of the measurement profiles used in the calculation, ethane and halon-1211 mixing ratios as a function of theta are shown in Fig. 4. We only use the ER-2 WAS measurements above 350 K, and averages are taken over each 10 K layer. The BL mixing ratios χ_{io}, based on the optimized K, y_{pTR} and y_{pNA}, for each theta average layer are shown by the colored symbols at 305 K. Note that for a trace gas in temporal decline, such as halon-1211, the BL mixing ratios from higher theta levels and older ages will have larger values since the air will have originated from the surface at a time when halon-1211 mixing ratios were larger than during the time of the mission. Ethane is also in decline, but, as shown in Fig. 2, the NA BL mixing ratios are much larger than the tropical BL mixing ratios. In this case, the higher theta levels also correspond to a more tropical source of air with low enough mixing ratios compared to the NA source that this shift in source region offsets the decline in time. Thus, the ethane BL mixing ratios for higher theta levels are smaller compared to those from lower theta levels: just the opposite as for halon-1211.

As an example of the method, Fig. 5a shows the $\mu(\tau)$ curves and age spectra for the 380 K level. A range of $\mu(\tau)$ curves and associated age spectra is shown along with the $\mu^*(\tau)$ values from the measurements over a range of source region combinations. The initial lifetimes associated with each of the μ^* values are based on those found at the 370 K level. The best fit based on the minimum value of D is shown by the dark blue line, and the adjusted τ_i values are shown in red. Those trace gases primarily destroyed by OH in the tropical troposphere generally have increased τ_i values after the adjustment, and those trace gases primarily destroyed by photolysis generally have decreased τ_i. This is consistent with pathways to a higher theta level in the UTLS encountering longer OH local lifetimes and shorter photolytic lifetimes. The six trace gases in the inset plot that decrease in lifetime are all photolytically destroyed in the stratosphere. The corresponding best-fit total age spectra are shown by the dark blue line, and the age spectra from the tropical and NA surface are shown in Fig. 5b. The age spectra from the different source regions have very different modal and mean ages. After an initial iteration of the method was performed, an adjustment was made to the average theta profiles following the calculation with the individual measurements, as described below and in Sect. S1. This adjustment is especially important for the shortest-lived trace gases, such as ethane shown in Fig. 4, which have a number of highly elevated mixing ratios below 400 K due to pollution sources, as described in Sect. 4.2.

4   Results

4.1   Average theta profiles

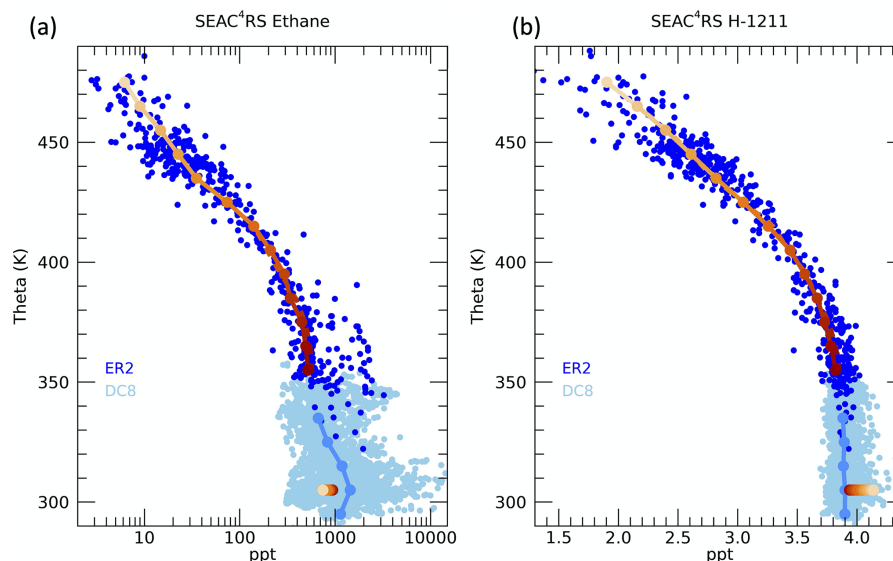With the methods described above applied to the average theta profiles of SEAC[4]RS measurements, we derive a range

Figure 4. Profiles of **(a)** ethane and **(b)** halon-1211 during the SEAC4RS mission as measured by the WAS instrument on the ER-2 (dark blue circles) and on the DC-8 (light blue circles). Theta averages for each 10 K interval are indicated by the solid lines, with dark to light orange symbols representing the theta level for the ER-2 measurements and light blue for the DC-8. The boundary layer values (χ_{io}) are indicated by the circles at 305 K, with orange shading corresponding to the associated theta level in the ER-2 average profile.

of UTLS transport characteristics in the summer NAM region. The $\mu(\tau)$ curves, age spectra and source latitude distributions for all the theta layers are shown in Fig. 6, and the path-integrated lifetime profiles of each trace gas are shown in Fig. 7. This combination of transport quantities has not previously been derived from in situ UTLS trace gas measurements in any study that we are aware of. Figure 6a includes the $\mu(\tau)$ curves based on the idealized trace gases and the $\mu^*(\tau)$ values at each theta level as colored symbols. Each of the measured trace gases follows a unique path as a function of theta on the $\mu(\tau)$ plot based on destruction source and growth history.

The age spectra from the NA and tropical surfaces (Fig. 6b, d) show the change from rapid-timescale (days) NA influence in the lowest theta layers to long-timescale (months to years) tropical influence in the higher theta layers. The NH age spectrum for the 350–360 K layer has a modal age of ~ 2.5 d, similar to the 2 d modal age derived from measurements in the UT of the convectively active tropical Pacific (Luo et al., 2018). The modal age from the tropical surface is ~ 2 months in the lowest theta layers and 3–4 months in the highest layers. Profiles of the modal and mean ages from the theta average results are shown in Fig. 10 in the following section for the individual measurement calculation.

The surface source latitude distributions for each theta layer reveal the expected transition from local influence in the lower theta layers, below 400 K, to deep tropical surface influence in the higher theta layers above 420 K. The NA source distributions peak in the 40–50° N range for the sampled UT and move south to 30–40° N in the tropopause

region and the LS. The distributions are scaled by the NA and tropical source fractions, F_{NA} and F_{TR}, profiles of which are shown in the next section in Fig. 10. NA source fractions are 0.4–0.5 below 370 K, so the peaks at 40–50° N are of similar size as the tropical peaks, while above 420 K the NA fractions are less than 0.2, so the tropical peaks at 0–10° N are dominant for those layers.

The path-integrated trace gas lifetimes τ_i, consistent with the optimal age spectra and source latitude distributions in Fig. 6, are shown in Fig. 7. As described in the Methods section, the initial values of τ_i in the lowest 350–360 K layer are listed in Table 1 for each trace gas. However, when an optimum value of K is found, the τ_i values are adjusted so that the values shown in Fig. 7 do not necessarily match those in Table 1 in the 350–360 K layer. In each subsequent higher theta layer, the τ_i values are adjusted based on the optimal $\mu(\tau)$ curve in that layer such as shown for the 380–390 K layer in Fig. 5. The τ_i profiles reveal a number of interesting features that are generally consistent with what would be expected based on the different sink mechanisms and locations for each of the trace gases.

The shortest-lived trace gases have τ_i values that mostly increase with theta, as expected since they react with OH radicals that decrease with altitude caused by the decrease in water vapor. As the sampled air parcels move further from the troposphere in higher theta layers, the pathways of transport from the surface to those theta layers will include more regions with less OH and longer local lifetimes. The exceptions are propane and perchloroethylene (C_2Cl_4) below 400 K. The τ_i profiles for the short-lived trace gases can be influenced by
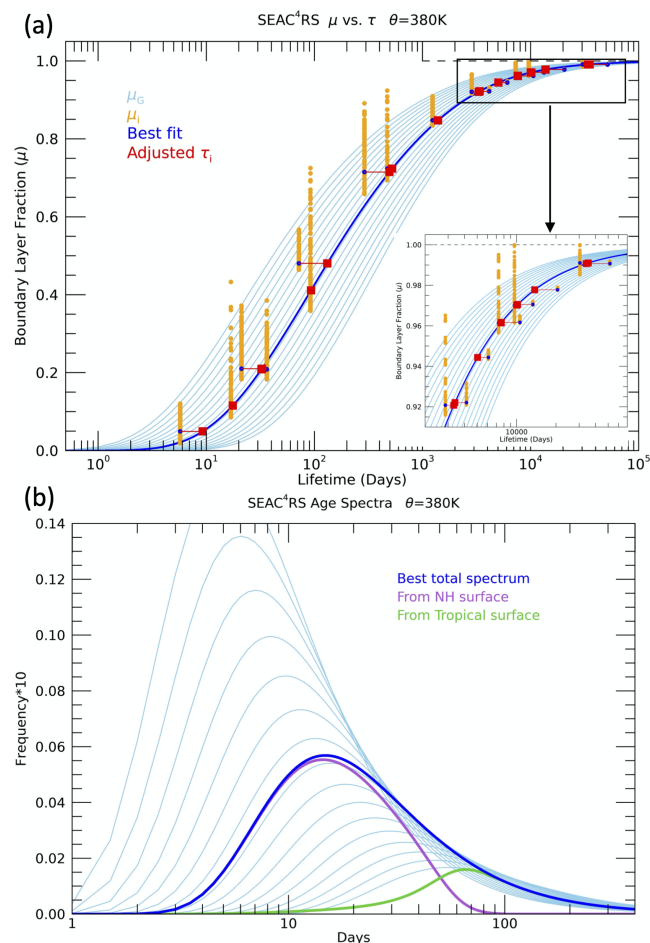
Figure 5. (a) BL fractions calculated for a set of idealized trace gases (μ) from age spectra with different values of the parameter K (light blue lines in **a** and **b**) and from a set of 20 different trace gases measured during SEAC^{4}RS averaged in the 380–390 K layer (μ^*) (orange circles). The μ^* values are only shown for the BL mixing ratios (χ_{io}) calculated with the K value and age spectra with the best fit at this level (blue line). The blue circles show μ^* values with the source region combination that best fits the idealized $\mu(\tau)$ as well as the measured CO_2 (see text). The τ_i values are then adjusted so that each μ^* value falls exactly on the best-fit $\mu(\tau)$ curve (red squares). The inset plot in the lower right corner is an expansion of the lifetime range older than 2000 d. **(b)** Age spectra with the same range of K values as shown in (**a**) and the best-fit spectra (blue) corresponding to that shown in (**a**). The age spectra from the NA surface (25–60° N) (light purple) and the tropical surface (25° S–25° N) (light green) are also shown.

the number of tropical vs. extratropical sources since their local lifetimes vary significantly with latitude. Propane, ethyne, ethane and the butanes have local lifetimes estimated to be roughly a factor of 2 longer in the NH subtropics compared to the tropics (Luo et al., 2018; Tang et al., 2007). But the details of how the local lifetimes of these trace gases vary with latitude and season are not well known, so it is diffi-

cult to clearly attribute the propane and perchloroethylene τ_i decreases below 400 K.

The HFCs and HCFCs also have increasing values of τ_i with higher theta due to the dominance of OH destruction in the troposphere for these species (WMO, 2018). Therefore, the τ_i profiles of these species generally have relatively smaller values at the lowest theta levels compared to the CFCs and cross over to have relatively larger values than the CFCs at the highest theta levels where the photolytic destruction of CFCs becomes the dominant loss process. The trace gas with the longest stratospheric lifetime of any used in this study is HFC-134a at 267 years (WMO, 2018), and it has the largest value of τ_i in the 470–480 K layer at $\sim 3.5 \times 10^4$ d or ~ 100 years. In the 350–360 K layer the τ_i value for HFC-134a is $\sim 3.5 \times 10^3$ d or ~ 10 years, so the τ_i value for this trace gas increases by an order of magnitude over the sampled UTLS region. The 10-year value of τ_i for HFC-134a in the UT is consistent with the local lifetime estimates of Chelpon et al. (2021) of ~ 5 years in the tropical troposphere and 15–20 years over the whole troposphere (WMO, 2018; Chelpon et al., 2021).

The CFCs are destroyed by photolysis in the stratosphere, so all of their τ_i values are very large in the UT and decrease with increasing theta as more transport pathways pass through the stratospheric loss regions. Halon-1211 has loss from both OH in the troposphere and photolysis in the UTLS, so it has a τ_i profile that decreases less rapidly than the CFCs (Chipperfield et al., 2013; WMO, 2018). Chloroform ($CHCl_3$) and methyl bromide ($CHBr_3$) also have both OH and photolytic loss but much shorter tropospheric lifetimes (2–3 months and 2 years) relative to their stratospheric lifetimes (1–2 years and 33 years) compared to halon-1211 (10–15 and 30–40 years) (Saltzman et al., 2004; Chipperfield et al., 2013; WMO, 2018). This ratio of stratospheric to tropospheric lifetimes of ~ 10 results in τ profiles of chloroform and methyl bromide with increasing values below 400 K as for the short-lived trace gases but decreasing values above 400 K, similar to the CFCs.

The contrast between the τ_i profiles of chloroform and HFC-152a clearly illustrates the effect of trace gases with somewhat similar tropospheric lifetimes but much different stratospheric lifetimes. The τ_i values for these two trace gases are basically identical in the 380–400 K layer, but HFC-152a τ_i values increase above this level, while those of chloroform decrease. The difference in τ_i reaches a factor of 3 above 460 K, and this reflects the relative stratospheric lifetimes of 33 years for HFC-152a compared to 1–2 years for chloroform (WMO, 2018).

It is important to note that features of the τ_i profiles described above were not prescribed ahead of time in the optimization method. An initial constraint on the τ_i values was required for the lowest theta layer, but even in that layer the τ_i values were allowed to vary based on the best-fit $\mu(\tau)$ curve. Thus, while the absolute values of τ_i have some uncertainty, the relative values and theta profile shapes are robust and help
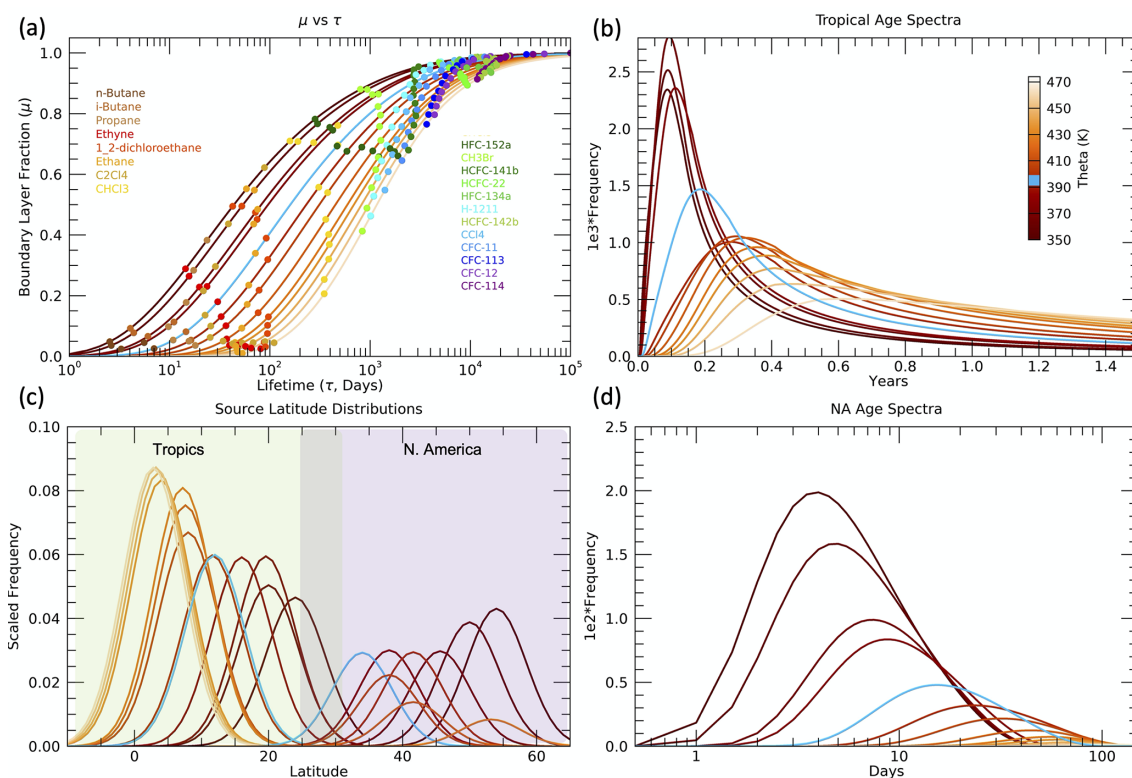
Figure 6. (a) Boundary layer fractions (μ) vs. path-integrated lifetimes (τ) for each theta layer from 350–470 K in 10 K intervals. The solid lines are the $\mu(\tau)$ relationships based on the best-fit age spectra shown in **(b)** and **(d)** and as described in the Methods section. The colored symbols are the $\mu^*(\tau)$ values based on the 20 trace gases listed in the legend and Table 1. **(b)** Tropical (g_{TR}) and **(d)** NA (g_{NA}) source region optimal age spectra for each theta layer. **(c)** Tropical (L_{TR}) and NA (L_{NA}) source region latitudinal distributions associated with the age spectra and used to calculate the μ^* values shown in **(a)**. The latitudinal distributions are scaled by the fractions of air that originated in the tropical (F_{TR}) and NA (F_{NA}) source regions in each theta layer. The light blue lines in each plot represent the distributions for the 390–400 K layer.

Figure 7. Profiles of the path-integrated trace gas lifetimes (τ_i) derived from the theta average profiles.

confirm the validity of the method as well as all of the surface time series in relation to the ER-2 UTLS measurements.

4.2 Individual measurement locations

Following the calculation of age spectra and other transport diagnostics based on the mean theta profiles, we performed the same method on each set of measurements taken at the individual sampled locations as shown in Figs. 1 and 3. A minimum of 10 species from Table 1 must have been measured from WAS at a location for the calculation to be performed. We initialize these calculations with the age spectra and trace gas lifetimes derived from the average theta profiles for the layers in which the individual measurements were taken. As will be shown below, the calculation with the average theta profiles is essential to provide context and a means to accommodate the wide range of individual measured mixing ratios in the method.

An immediate issue with the individual measurements is the occurrence of UTLS mixing ratios larger than the BL mixing ratios, which would result in $\mu^* > 1$. This violates
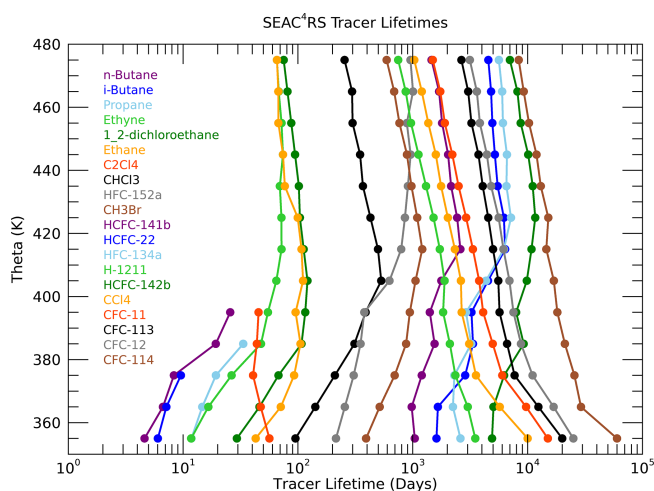
the assumption of the method as described by Eq. (3), where $\mu = 1$ is only defined for $t' = 0$ in the boundary layer. Equation (1) excludes the case in which $\mu > 1$. The range of measured UTLS mixing ratios is expected based on the range of measured mixing ratios in the free troposphere and BL by the DC-8 as shown, for example, for ethane in Fig. 4 and the butane species in Fig. S1 in the Supplement. Our assumption is that the relatively large mixing ratios below 420 K, especially when $\mu^* > 1$ but even when $\mu^* < 1$ but falls outside the expected $\mu(\tau)$ values, are primarily driven by NA source variability since transport alone cannot cause such high values. Above 420 K, the spread is primarily driven by transport variability since the NA BL has a relatively small influence at those locations.

A strength of this method, including the wide range of trace gases used here, is that outliers from the $\mu(\tau)$ curves are readily apparent and the magnitude of adjustments necessary to bring the outliers in line with the other trace gases can be well approximated. We make the assumption that outliers are the result of "polluted" source regions, so we perform several steps to identify and adjust the boundary conditions with a scaling factor S for the trace gases with enhanced UTLS mixing ratios (see Sect. S5 for details). The result of this scaling is that essentially all of the available measurements can be used in the calculation, and we are able to quantify a range of polluted source regions to the NAM UTLS.

An example of the BL scaling and age spectra optimization for an individual location with a relatively polluted BL source for certain trace gases is shown in the $\mu(\tau)$ relationships in Fig. 8. There is a wide spread in the initial $\mu_i^*(x)$, with values greater than 1 for a range of trace gases from propane and ethane to HFCs and CCl$_4$, while several other trace gases, such as 1,2-dichloroethane, CHCl$_3$ and CFC-113, have values close to the $\mu(\tau)$ values for the theta layer average indicated by the dotted line.

Following the $S_{\text{inorm}}(x)$ scaling, the $\mu^*(x)$ values decrease for many of the short-lived trace gases, as indicated by the upward triangles (Fig. 8a), and there are no remaining values of $\mu^*(x) > 1$ for these species. However, for the longest-lived trace gases (Fig. 8b) the $S_{\text{inorm}}(x)$ scaling has no effect because the condition of $\chi_{\text{inorm}}(x) \geq 1.2$ was not met for any of these species (the upward triangles are not shown since there is no change from the initial values). For the longest-lived species the $S_{i\mu}(x)$ scaling (left-facing triangles) brings the elevated $\mu^*(x)$ values below 1, so the optimization can be performed. The left-facing triangles are not shown for the shortest-lived species since there is no change from the $S_{\text{inorm}}(x)$ scaling. Three of the trace gases (propane, HFC-22 and CFC-11) are affected by the $S_{i\tau}(x)$ scaling (upside-down triangles) since they fall in the green shaded area of Fig. 8, which indicates that τ_i is outside the range expected for this theta layer.

For the location shown in Fig. 8 it could easily be assumed that with relatively large measured mixing ratios of short-lived trace gases such as n-butane, propane and ethane the
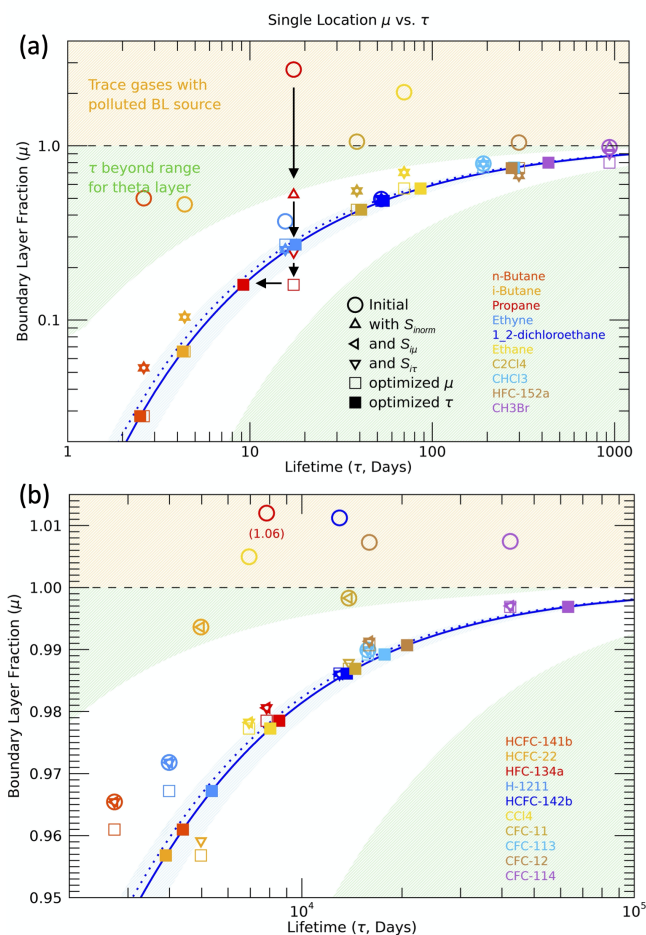

Figure 8. Boundary layer fraction (μ) vs. path-integrated lifetime (τ) for a single SEAC^{4}RS measurement location near the tropopause ($\theta = 362$ K, 29° N). The 10 shortest-lived species are shown in **(a)**, and the 10 longest-lived species with a narrowed μ range are shown in **(b)**. The orange shaded region where $\mu > 1$ indicates a polluted BL source region, while the green shaded region indicates where the estimated τ values fall outside the expected range for the theta layer. The $\mu - \tau$ relationship for the theta layer average is indicated by the dotted blue line and the best fit for this individual location by the solid blue line. The symbols represent adjustments made to $\mu^*(x)$ by the various scaling factors applied to the boundary conditions χ_{io} and from the optimization (see text).

dominant age of the sampled air parcel would be very short, essentially hours or days since it was convectively transported to this UT location. However, with this method we find an age spectrum with a modal age of 5 d and a mean age of roughly half a year for this location. These timescales are necessary to explain the $\mu^*(\tau_i)$ values of trace gases such as 1,2-dichloroethane, CHCl$_3$, halon 1211 and CFC-113, which lie almost exactly on the $\mu(\tau)$ curve for the theta layer average. There is no way that trace gases such as these with τ_i ranging from several months to 50 years could have values of μ^* significantly less than 1 as they do, without frequency in
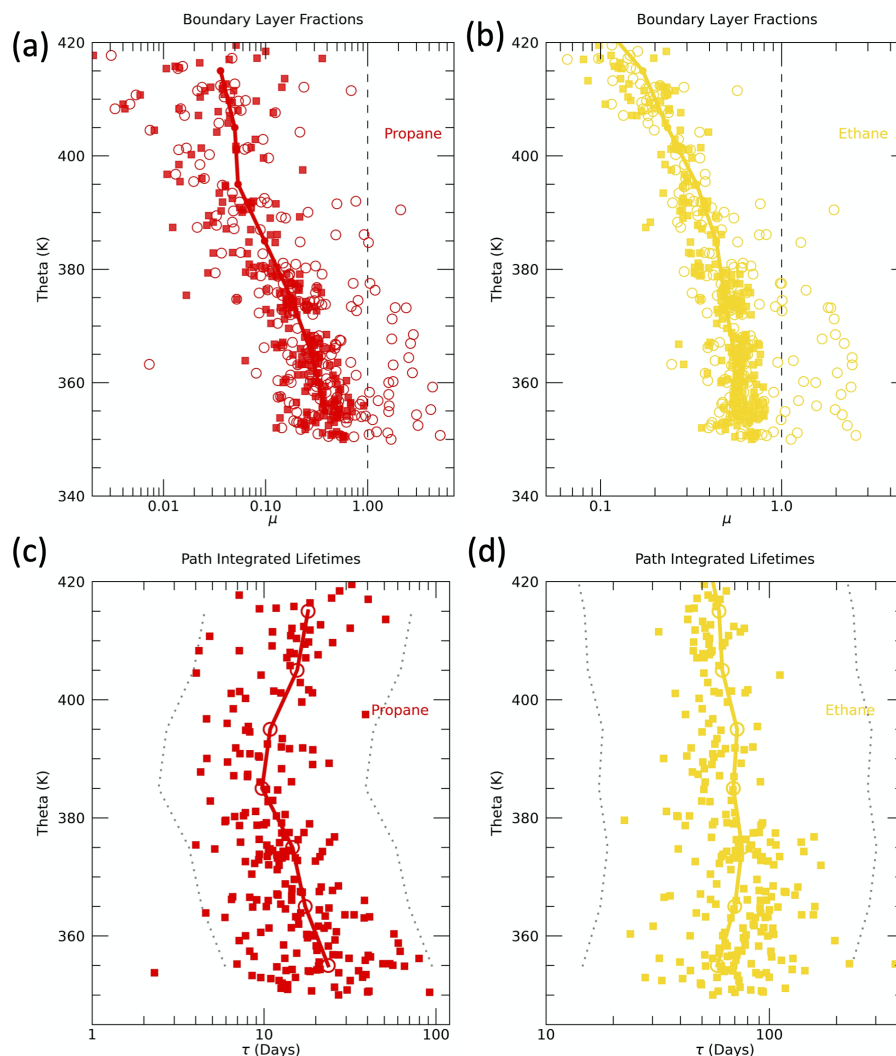
Figure 9. Boundary layer fractions (μ^*) vs. theta for **(a)** propane and **(b)** ethane for the theta profile averages (solid lines), initial estimates of μ^* (open circles) and final estimates of μ^* (solid squares) following scaling of BL time series and optimization calculation (see text). Path-integrated lifetime (τ) profiles for **(c)** propane and **(d)** ethane based on the average theta profiles (solid lines, open circles) and the individual measurement locations (solid squares). The constraint limits used in the calculation of the individual location age spectra are shown by the dotted lines, representing lifetimes a factor of 4 smaller or larger than the average profile.

the age spectra representing timescales from weeks to years. There is the possibility that the τ_i values for these four trace gases are overestimated or their BL time series are overestimated such that their μ^* values are too low. But different trace gases exhibit the average theta layer $\mu(\tau)$ values for different air parcels, and the initial calculation with the average theta profiles establishes the framework among the trace gases that would reveal systematic errors in BL time series, for example. So, while this air parcel does have a component of the age spectra representing transport timescales of hours to days, this is relatively small compared to the longer transport timescales of weeks to months. And the explanation for the relatively high measured mixing ratios of a number of short-lived trace gases, which becomes clear with this

method, is that the air parcel was influenced by transport from polluted BL locations with highly elevated levels of certain trace gases.

Examples of the individual measurement location outlier identification technique are shown in the profiles of μ^* and τ for propane and ethane (Fig. 9). Both propane and ethane initially have a significant number of values of $\mu^* > 1$ (open circles), as expected from the normalized mixing ratios shown in Fig. S7. Following the scaling of outliers and optimization for the individual measurements, the final estimates have no values of $\mu^* > 1$ and much less spread around the theta average profile, especially on the high end of the values. The τ profiles have essentially the opposite behavior between the initial and final estimates since we initialize the individual
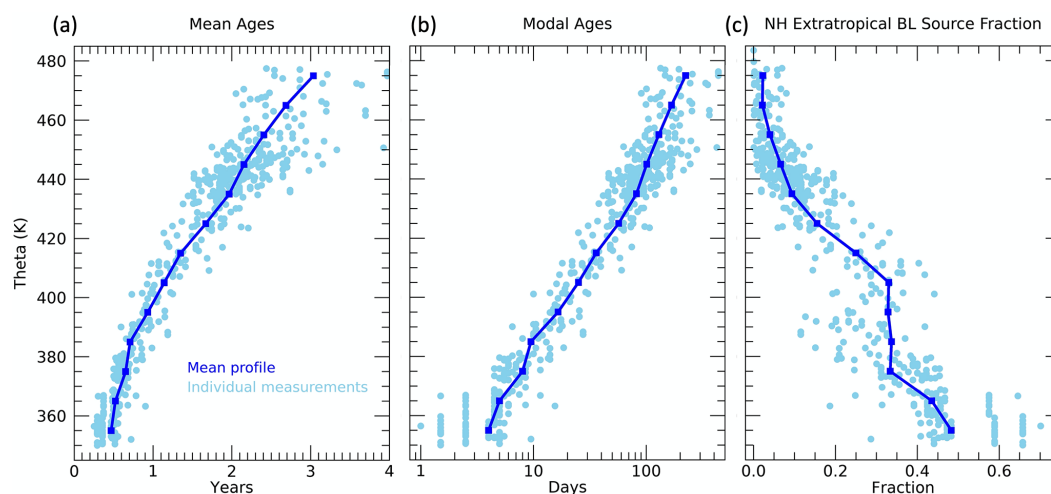
Figure 10. Profiles of **(a)** mean age, **(b)** modal age and **(c)** F_{NA} as a function of theta. Results from the theta average profiles are shown as dark blue lines and symbols, and those from the individual measurement locations as light blue symbols.

locations with the values from the theta average profile. This means that all of the individual trace gases in a theta layer will initially have the theta average $\tau_i(z)$ values. After the scaling and optimization, the individual $\tau_i(x)$ values are estimated from the best-fit $\mu(\tau)$ curves. This introduces a spread in the $\tau_i(x)$ values that is constrained to be within a factor of 4 greater or smaller than the $\tau_i(z)$ values. For the longest-lived trace gases this spread is much less than a factor of four. Almost all of the values of $\tau_i(x)$ lie within the limits shown by the dotted lines in Fig. 9 with the exception of a couple of propane values. In these cases, the propane BL time series could not be scaled effectively and they remain outliers. But in nearly all locations the $\tau_i(x)$ values are able to be constrained for all of the trace gases. The constraint limits are arbitrary, but after some experimentation these limits appear to account for clear outliers while also allowing variability within each theta layer that is expected due to transport variability.

In the calculation of μ^* as shown in Eq. (13), the scaling was performed on the total χ_{io} values. But what this scaling implies is that there is a relatively polluted surface region that impacted the measured mixing ratios in the UTLS. The polluted surface region was almost certainly in NA for two main reasons. One is that we know there are relatively large mixing ratios of all of the trace gases in this study in the lower troposphere over NA as measured during SEAC[4]RS (Figs. 4 and S1) that come from various pollution sources. And two, while there are significant pollution sources in the tropics, they will most likely be at longitudes far from where SEAC[4]RS flights sampled the UTLS, such as Asia, and would thus be mixed with the background tropical troposphere before entering the sampled UTLS.

Assuming the pollution sources that affected the sampled UTLS during SEAC[4]RS were from the NA only, the scaling factor should only be applied to the $\chi_{io\mathrm{NA}}$ in Eq. (11). Since

the scaling factors derived above relate to χ_{io}, to apply a scaling only to $\chi_{io\mathrm{NA}}$, we need to increase the scaling factor by the inverse of the fraction of air from NA. That is,

$$S_{i\mathrm{NA}}(x) = \frac{S_i(x)}{F_{\mathrm{NA}}(x)}, \tag{14}$$

where $S_i(x)$ is the scaling factor derived to apply to χ_{io} for trace gas i and measurement location x, and $S_{i\mathrm{NA}}(x)$ is the scale factor applied only to $\chi_{io\mathrm{NA}}$. As seen in Fig. 10, F_{NA} ranges from 0.2–0.6 for theta less than 410 K when the scaling is applied. Thus, the derived values of S_i are increased by factors of 1.6–5 to obtain the values of $S_{i\mathrm{NA}}$.

Following the scaling of $\chi_{io\mathrm{NA}}$, we compute optimized K, associated age spectra and surface source latitudes for each individual WAS ER-2 measurement location. Profiles of the mean ages, modal ages and NA source fractions are shown in Fig. 10. The mean ages range from several months in the UT to several years in the LS with much more spread in values at the higher theta levels, primarily driven by a latitudinal gradient as seen in Fig. 11. The modal ages range from days in the UT to months in the LS with a large latitudinal gradient above 450 K.

The values of F_{NA} (Figs. 10 and 11) range from 0.2–0.6 in the UT, which means 20 %–60 % of the air in the sampled parcels originated from the NA surface north of 25° N, to less than 0.1 in the LS above 450 K. From 370–410 K the theta average F_{NA} values are nearly constant at ~ 0.3. This is related to the transition of the source region scaling factor timescale, t_{f}, from 50 to 150 d over this theta range. As the value of t_{f} increases, F_{NA} will increase if the age spectrum remains the same since more of the air at ages less than t_{f} will have come from the NA surface. However, since the mean age increases with theta the number of age spectra in the 50–150 d range decreases with theta, which roughly offsets the increase in the value of $f(t)$ in that age range. The individual
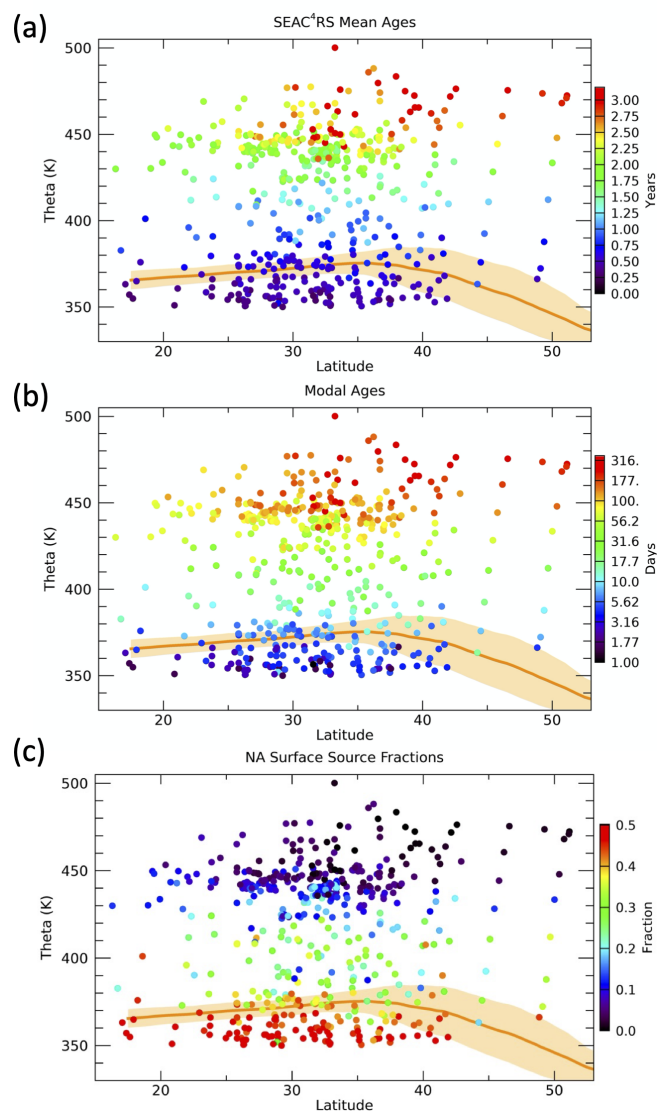
Figure 11. Latitude vs. theta distributions of the mean age, modal age and NA surface source fractions for each aircraft measurement location. Tropopause regions based on MERRA2 products are indicated by the orange shading and solid line.

measurements show a wide range of values of F_{NA} in the 380–400 K layer from 0.1–0.4. The relatively low values of F_{NA} in this layer are consistent with horizontal intrusions of tropical air into the LS above the subtropical jet, typically due to Rossby wave activity in the spring (Pan et al., 2009).

Mean ages in the UTLS have been estimated from in situ measurements and model output in many previous studies (e.g., Boenisch et al., 2009; Diallo et al., 2012; Konopka et al., 2015; Ploeger and Birner, 2016; Hauck et al., 2020). The range of values calculated here is very similar to those from the same region and season in previous studies. For instance, in Ploeger and Birner (2016), CLaMS model output has mean ages during summer in the 20–40° N region that

range from ∼ 1–3 years between 350 and 500 K. This provides some confidence that the mean age results shown here fall within expected values.

The modal ages can also be compared to previous estimates, but this quantity is much less commonly shown over a range of latitudes and vertical levels and has not been calculated from the surface based on measurements that we are aware of. In Ploeger et al. (2019) the modal age based on CLaMS output from 20–40° N and 400 K in summer is 4–5 months, which is considerably longer than the 10–30 d modal ages from our calculation. The model results are based on zonal averages, however, so the convectively active NAM region would be expected to have shorter modal times due to the rapid convective transport from the surface. A more recent study using CLaMS output (Yan et al., 2021) focused on transport from different surface latitude regions and found somewhat faster (∼ 3 month) modal times for transport from the NH extratropical surface to the NH extratropical UTLS in summer. This study again only shows zonal mean results, so it is likely that the modal times would be even shorter in the NAM region.

The F_{NA} distributions can be compared to those from previous studies that calculated UTLS source region fractions from model output. In Orbe et al. (2015), the tropics were defined as 10° S–10° N and the NH extratropics north of 10° N, so the F_{NA} values should be relatively large and the F_{TR} relatively small compared to our results. That is roughly consistent with values of F_{TR} in that study, which range from 0.2 in the summer UT to 0.6 in the LS above 100 hPa or ∼ 400 K, and values of F_{NA} from 0.7 in the UT to 0.3 in the LS. The main difference is the higher F_{NA} values through the LS that likely relates to the wider source region definition. Another study with this type of model surface source analysis is Yan et al. (2021) wherein the tropics were defined as 30° S–30° N, so the F_{NA} values should be relatively small compared to our results. In that study, F_{NA} ranges from 0.06 in the NH summer UT to 0.02 in the LS, while F_{TR} ranges from 0.94–0.97. These are clearly much smaller values of F_{NA} compared to our results, and it is not clear if the source region definitions are different enough to explain the discrepancy. The differences could be due in part to an underestimation of the convective influence in the NAM region on the UTLS in the models. Further comparisons of source region fractions defined from UTLS measurements and models would be a useful new diagnostic of model transport, and we intend to perform such analysis in a future study.

The BL source peak latitudes (y_{TR}, y_{NA}) for the individual UTLS measurement locations are a unique aspect of this calculation (Fig. S4). Figure 12 shows profiles of y_{TR} and yNA scaled by the fractions of air from each region, F_{TR} and F_{NA}. Only locations with CO_2 measurements are shown since without those measurements the source latitudes are much less well constrained. The source region fractions show that the largest contribution of the North American BL to the sampled UTLS is from 40–55° N. The correspondence of the
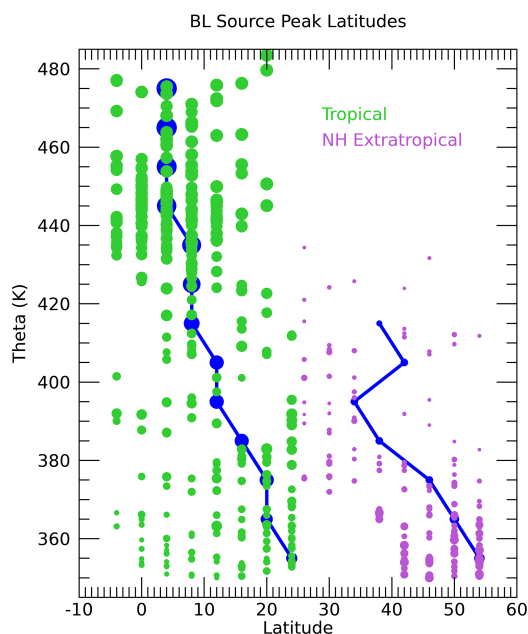
Figure 12. BL source peak tropical (y_{TR}, green) and NA (y_{NA}, purple) latitude profiles. The symbols are sized based on the value of F_{TR} for the tropical latitudes and F_{NA} for the NA latitudes. The results for the theta average profiles are shown by the dark blue lines.
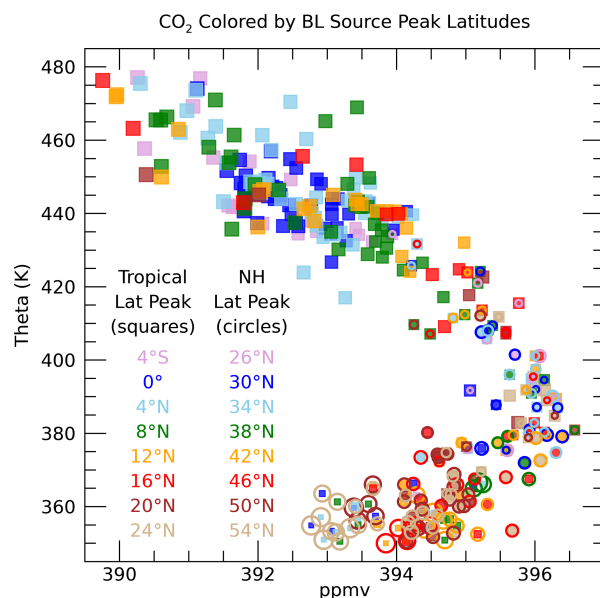

Figure 13. Individual measurement CO_2 profile colored by the BL source peak latitudes in the tropics (squares) and NA (open circles). The symbols are colored by the source latitudes in each region, as indicated by the legend, and sized by the values of F_{TR} and F_{NA} for the tropical and NA symbols, respectively.

source latitudes to the CO_2 mixing ratios is shown in Fig. 13. Below 370 K, the lowest CO_2 mixing ratios come from the highest latitudes of 50–54° N. This follows from the large latitudinal gradient in CO_2 in the BL over NA during the summer as shown in Fig. S2. Since the age spectra below 370 K are heavily weighted toward the most recent several weeks before the flights, only the highest latitudes have mixing ratios low enough during that time to account for the lowest measured CO_2 mixing ratios. The higher the measured CO_2 mixing ratio, the further south the source fractions.

The tropical contributions are relatively small for theta lower than 370 K and spread across a range of tropical latitudes. The smallest symbols shown in Fig. 12 have the most uncertainty since they represent small values of F and thus have a small influence on the measured set of trace gases. The 370–400 K layer is a transition zone going from equal contributions from NA and the tropics to a more tropical source. The wide range of source latitudes, especially in the 370–380 K layer, is reflected by the range of measured CO_2 mixing ratios in this part of the UTLS as shown in Fig. 13. The NA source latitudes continue to be inversely related to the measured CO_2 as in the lower theta levels, while the tropical source latitudes continue to be less well correlated with the measured CO_2. This is mostly due to the much larger summertime latitudinal gradient of CO_2 north of 30° N compared to the tropical latitudes, which results in more leverage over the measured CO_2 by the high-latitude source region compared to the tropics. The largest measured CO_2 mixing ratio

in the UTLS of 396.5 ppm at 380 K is shown to best fit an NA source peak latitude of 38° N and a tropical peak latitude of 20° N.

Above 400 K, there is a transition to tropical latitudes as the primary source region to the measured UTLS. The NA symbols are very small above 400 K and disappear altogether above 440 K, which indicates values of $F_{NA} < 0.2$ at those locations. The tropical source latitudes shift to the south, near the Equator, with higher theta. Above 420 K the tropical source latitudes are 4° S–16° N with the theta average profile at 8° N, which is roughly the position of the ITCZ.

We can also look at the distributions of the source latitudes from each region as a function of the measurement location in latitude and theta as shown in Fig. 14. The symbols are sized as in Figs. 12 and 13 to make the contribution from each region at the different locations clear. The shift from northern subtropical to deep tropical source latitudes with increasing theta is apparent, as in the previous figures. There is no significant latitudinal gradient in the tropical source latitude within each theta layer. Below 380 K, the largest sized symbols generally have source peak latitudes north of 20° N. This can also be seen in Fig. 12 and generally matches the average theta profile tropical peak latitude of 20° N in the lower layers.

The NA source peak latitude distribution shows the previously noted shift from high-latitude sources in the lowest theta layers to lower-latitude sources above 370 K where F_{NA} becomes small. There is an interesting latitudinal gradient in the extratropical source latitudes below 370 K such that at the
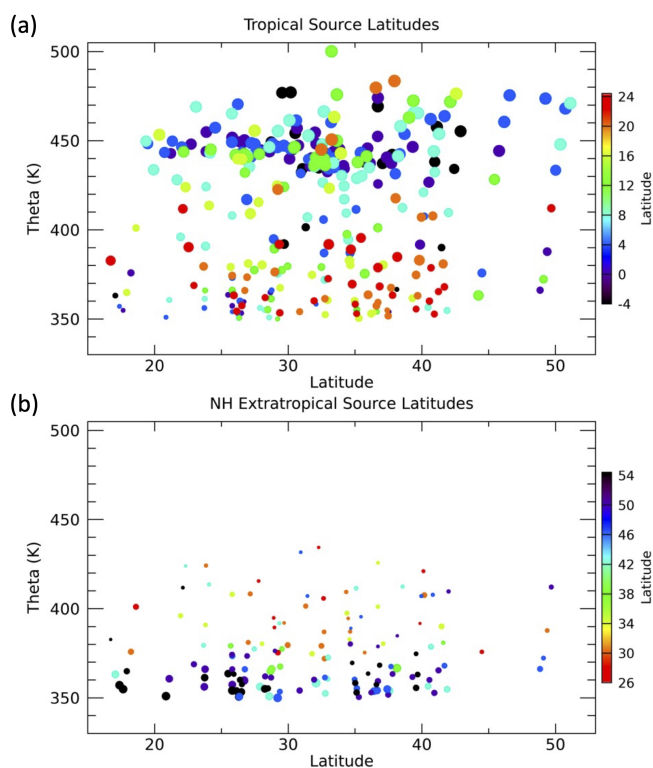
(a)

(b)

Figure 14. Individual measurement locations as a function of latitude and theta colored by peak BL source latitude and sized by the values of F_{TR} and F_{NA} for the **(a)** tropical and **(b)** NA plots, respectively. Only locations where $F > 0.2$ and CO_2 measurements were available are shown in each plot.

Figure 15. Ozone mixing ratios vs. modal age for the individual measurements (light blue circles) and theta average profiles (dark blue line and circles) from the SEAC[4]RS mission.

more southern sampled latitudes the NA sources are from the most northern locations. The anticyclonic circulation in the NAM UT region can transport air across a wide range of latitudes within days as seen in previous trajectory studies such as Herman et al. (2017), which was focused on the SEAC[4]RS mission. In that study, convective overshooting regions were shown to influence sampled UTLS air masses up to a week or so later and 10–20° in latitude away.

5 Discussion

The methods and results described here take advantage of the wide range of trace gas measurements taken during the SEAC[4]RS mission, as well as from surface sites around the world, to reveal a unique set of transport characteristics of the summertime UTLS over North America. This work builds on the techniques and ideas of many previous studies, especially on recent studies that have focused on maximizing the transport information derived from a suite of trace gas measurements (Luo et al., 2018; Hauck et al., 2019, 2020; Podglajen and Ploeger, 2019; Chelpon et al., 2021). This advancement in our knowledge of more detailed transport aspects of the
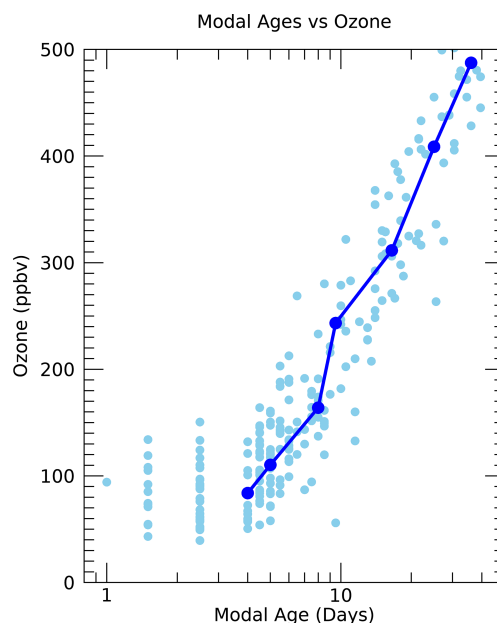
UTLS from measurements is important to better constrain global climate models and reanalysis products in this region.

This work is ideally a step along the way towards more comprehensive measurement-based transport diagnostics utilizing the many other in situ and remote measurement datasets that exist today and those to come from future missions. The results shown here are by no means the exact answers for each transport diagnostic at each measurement location. We have made a number of assumptions in the method, which are described in the main text and the Supplement, that could change individual results somewhat if different choices were made. For instance, the partitioning of the source regions into the tropics and NA neglects the potential contribution from other extratropical source regions such as from the Asian monsoon. We know the Asian monsoon influences the boreal summer extratropical UTLS composition at all longitudes (e.g., Yu et al., 2017), so a complete description of surface source regions to the NAM UTLS would include Asia. Since we do not currently have sufficient surface measurement time series in Asia, we cannot include it as a separate source in this calculation. But in spite of the limitations in the method, the overall patterns and self-consistency of the results are robust to a range of different assumptions from those made here.

An important aspect that has not been discussed thus far is the seasonal cycle in transport. We have incorporated the seasonal cycle in the trace gas mixing ratio time series in the boundary layer, but we have not explicitly added a seasonal cycle to any of the transport diagnostics beyond what is revealed by the trace gas measurements. It has been shown in

many previous modeling studies and in the recent work of Hauck et al. (2019, 2020) and Podglajen and Ploeger (2019) that the seasonal cycle is a significant feature in the age spectra in the UTLS due to the seasonal cycle in transport in this region. These studies show that available trace gas measurements in the UTLS are generally not sensitive enough to the seasonal cycle to reveal the seasonal features seen in age spectra from model output. A technique to account for the seasonal cycle revealed by models is to essentially parameterize a seasonal cycle into the age spectra and otherwise let the measurements define the rest of the spectra shape. We did try this technique with our method and found that the results were very similar for all of the transport diagnostics. Since the focus of this study is on measurement-based diagnostics we decided to leave the model-derived seasonal cycle parameterization out of the method. Thus, for this reason, the older parts of the age spectra shown here are likely not technically correct. In future work, as a means to better compare the measurement-based transport diagnostics to those from model output, we plan to include the parameterized seasonal cycle in our results.

Another qualification of this method is that it cannot include trace gases with significant production in the atmosphere such as ozone. But we can use the transport diagnostics derived from the other trace gases to help interpret the simultaneously measured ozone in the UTLS. For instance, Fig. 15 shows the measured ozone mixing ratios from SEAC^{4}RS at the WAS measurement locations as a function of the modal age. The modal age could be used as an indicator of recent convective injection of air from the surface to the UTLS since a short modal age (days) should correspond to the time of convective injection. We see from Fig. 15 that for modal ages of less than a week, essentially all of the ozone mixing ratios are less than 200 ppb, with most of them below 100 ppb. For modal ages greater than a week there is a sharp increase in ozone mixing ratios. This is consistent with the expected relationship between recent convective injection and relatively low ozone mixing ratios in the UTLS since the BL ozone is typically much lower than the background values in this region.

6 Summary

We have calculated age spectra, path-integrated lifetimes and surface source regions in the UTLS over North America during the summer monsoon season using in situ trace gas measurements primarily from the WAS instrument on the ER-2 aircraft during the SEAC^{4}RS campaign. This range of transport diagnostics has not previously been produced solely from measurements for this region of the atmosphere. The results are shown to be broadly consistent with those from previous modeling and measurement studies as well as with our general understanding of large-scale transport and the photochemistry of the trace gases used.

We show that the mean ages in the sampled region range from several months to several years and the modal ages from days to months. The gradients in the ages are primarily a function of theta, but above 450 K there are also substantial latitudinal gradients such that the oldest air was found at the highest latitudes. Convective injection from the local North American surface was shown to be a significant source of air to the NAM UTLS below 380 K, with a transition to mostly tropical sources of air in the summer stratospheric overworld. CO_2 in particular is useful for identifying surface source regions of air in the UTLS, and its use in combination with the wide range of other trace gases is a unique aspect of this study.

The comprehensive utilization of the information deduced from a wide range of simultaneously measured trace gases, following on the methods and ideas from recent studies (e.g., Luo et al., 2018; Hauck et al., 2019, 2020), is an important step forward in our understanding of trace gas distributions in the UTLS; ideally, it can be done with different datasets in other locations and seasons and lead to improvements in chemistry–climate model transport in the UTLS.

Author contributions. EAR designed and carried out the calculations and wrote the paper. ELA and SS provided the aircraft measurements. SC, LP, HB and KHR provided conceptual support and paper suggestions.

Review statement. This paper was edited by Gabriele Stiller and reviewed by two anonymous referees.

References

Andrews, A. E., Boering, K. A., Daube, B. C., Wofsy, S. C., Hintsa, E. J., Weinstock, E. M., and Bui, T. P.: Empirical age spectra for the lower tropical stratosphere from in situ observations of CO_2: Implications for stratospheric transport, J. Geophys. Res., 104, 26581–26595, 1999.

Andrews, A. E., Boering, K. A., Wofsy, S. C., Daube, B. C., Jones, D. B., Alex, S., Loewenstein, M., Podolske, J. R., and Strahan, S. E.: Empirical age spectra for the midlatitude lower stratosphere from in situ observations of CO_2: Quantitative evidence for a subtropical "barrier" to transport, J. Geophys. Res., 106, 10257–10274, 2001.

Birner, B., Chipperfield, M. P., Morgan, E. J., Stephens, B. B., Linz, M., Feng, W., Wilson, C., Bent, J. D., Wofsy, S. C., Severinghaus, J., and Keeling, R. F.: Gravitational separation of Ar/N_2 and age of air in the lowermost stratosphere in airborne observations and a chemical transport model, Atmos. Chem. Phys., 20, 12391–12408, https://doi.org/10.5194/acp-20-12391-2020, 2020.

Bönisch, H., Engel, A., Curtius, J., Birner, Th., and Hoor, P.: Quantifying transport into the lowermost stratosphere using simultaneous in-situ measurements of SF_6 and CO_2, Atmos. Chem. Phys., 9, 5905–5919, https://doi.org/10.5194/acp-9-5905-2009, 2009.

Chelpon, S. M., Pan, L. L., Luo, Z. J., Atlas, E. L., Honomichi, S. B., and Smith, W. P.: Deriving tropospheric transit time spectra using airborne trace gas measurements: Uncertainty and information content, J. Geophys. Res., 126, 1–23, https://doi.org/10.1029/2020JD034358, 2021.

Chipperfield, M. P., Liang, Q., Strahan, S. E., Morgenstern, O., Dhomse, S. S., Abraham, N. L., Archibald, A. T., Bekki, S., Braesicke, P., Di Genova, G., Fleming, E. L., Hardiman, S. C., Iachetti, D., Jackman, C. H., Kinnison, D. E., Marchand, M., Pitari, G., Pyle, J. A., Rozanov, E., Stenke, A. and Tummon, F.: Multimodel estimates of atmospheric lifetimes of long-lived ozone-depleting substances: Present and future, J. Geophys. Res., 119, 2555–2573, https://doi.org/10.1002/2013JD021097, 2013.

Clapp, C. E., Smith, J. B., Bedka, K. M., and Anderson, J. G.: Identifying source regions and the distribution of cross-tropopause convective outflow over North America during the warm season, J. Geophys. Res., 124, 13750–13762, https://doi.org/10.1029/2019JD031382, 2019.

Class, T. and Ballschmiter, K.: Global baseline pollution studies, Anal. Chem., 327, 198–204, 1987.

Diallo, M., Legras, B., and Chédin, A.: Age of stratospheric air in the ERA-Interim, Atmos. Chem. Phys., 12, 12133–12154, https://doi.org/10.5194/acp-12-12133-2012, 2012.

Ehhalt, D. H., Rohrer, F., Blake, D. R., Kinnison, D. E., and Konopka, P.: On the use of nonmethane hydrocarbons for the determination of age spectra in the lower stratosphere, J. Geophys. Res., 112, D12208, https://doi.org/10.1029/2006JD007686, 2007.

Hall, T. M.: Path histories and timescales in stratospheric transport: Analysis of an idealized model, J. Geophys. Res., 105, 22811–22823, 2000.

Hauck, M., Fritsch, F., Garny, H., and Engel, A.: Deriving stratospheric age of air spectra using an idealized set of chemically active trace gases, Atmos. Chem. Phys., 19, 5269–5291, https://doi.org/10.5194/acp-19-5269-2019, 2019.

Hauck, M., Bönisch, H., Hoor, P., Keber, T., Ploeger, F., Schuck, T. J., and Engel, A.: A convolution of observational and model data to estimate age of air spectra in the northern hemispheric lower stratosphere, Atmos. Chem. Phys., 20, 8763–8785, https://doi.org/10.5194/acp-20-8763-2020, 2020.

Helmig, D., Rossabi, S., Hueber, J., Tans, P., Montzka, S. A., Masarie, K., Thoning, K., Plass-Duelmer, C., Claude, A., Carpenter, L. J., Lewis, A. C., Punjabi, S., Reimann, S., Vollmer, M. K., Steinbrecher, R., Hannigan, J. W., Emmons, L. K., Mahieu, E., Franco, B., Smale, D., and Pozzer, A.: Reversal of global atmospheric ethane and propane trends largely due to US oil and natural gas production, Nat. Geosci., 9, 490–495, https://doi.org/10.1038/ngeo2721, 2016.

Herman, R. L., Ray, E. A., Rosenlof, K. H., Bedka, K. M., Schwartz, M. J., Read, W. G., Troy, R. F., Chin, K., Christensen, L. E., Fu, D., Stachnik, R. A., Bui, T. P., and Dean-Day, J. M.: Enhanced stratospheric water vapor over the summertime continental United States and the role of overshooting convection, Atmos. Chem. Phys., 17, 6113–6124, https://doi.org/10.5194/acp-17-6113-2017, 2017.

Hodnebrog, O., Dalsoren, S. B., and Myhre, G.: Lifetimes, direct and indirect radiative forcing, and global warming potentials of ethane (C_2H_6), propane (C_3H_8), and butane (C_4H_{10}), Atmos. Sci. Lett., 19, e804, https://doi.org/10.1002/asl.804, 2018.

Holzer, M. and Hall, T. M.: Transit-time and tracer-age distributions in geophysical flows, J. Atmos. Sci., 57, 3539–3558, 2000.

Holzer, M. and Waugh, D. W.: Interhemispheric transit time distributions and path-dependent lifetimes constrained by measurements of SF_6, CFCs and CFC replacements, Geophys. Res. Lett., 42, 1–9, https://doi.org/10.1002/2015GL064172, 2015.

Jacobson, A. R., Schuldt, K. N., Miller, J. B., Oda, T., Tans, P., et al.: Carbontracker CT2019B, Model published 2020 by NOAA Earth System Research Laboratory, Global Monitoring Division, https://doi.org/10.25925/20201008, 2020.

Konopka, P., Ploeger, F., Tao, M., Birner, T., and Riese, M.: Hemispheric asymmetries and seasonality of mean age of air in the lower stratosphere: Deep versus shallow branch of the Brewer-Dobson circulation, J. Geophys. Res., 120, 2053–2066, https://doi.org/10.1002/2014JD022429, 2015.

Luo, Z. J., Pan, L. L., Atlas, E. L., Chelpon, S. M., Honomichl, S. B., Apel, E. C., Hornbrook, R. S., and Hall, S. R.: Use of airborne in situ VOC measurements to estimate transit time spectrum: An observation-based diagnostic of convective transport, Geophys. Res. Lett., 45, 13150–13157, https://doi.org/10.1029/2018GL080424, 2018.

Moore, F. L., Ray, E. A., Rosenlof, K. H., Elkins, J. W., Tans, P., Karion, A., and Sweeney, C.: A cost-effective trace gas measurement program for long-term monitoring of the stratospheric circulation, B. Am. Meteorol. Soc., 95, 147–155, https://doi.org/10.1175/BAMS-D-12-00153.1, 2014.

Olaguer Jr., E. P.: The distribution of the chlorinated solvents dichloromethane, perchloroethylene, and trichloroethylene in the

global atmosphere, Environ. Sci. Pollut. Res. Int., 9, 175–182, https://doi.org/10.1007/BF02987485, 2002.

Orbe, C., Holzer, M., Polvani, L. M., and Waugh, D.: Air-mass origin as a diagnostic of tropospheric transport, J. Geophys. Res., 118, 1459–1470, https://doi.org/10.1002/jgrd.50133, 2013.

Orbe, C., Waugh, D. W., and Newman, P. A.: Air-mass origin in the tropical lower stratosphere: The influence of Asian boundary layer air, Geophys. Res. Lett., 42, 4240–4248, https://doi.org/10.1002/2015GL063937, 2015.

Pan, L. L., Randel, W. J., Gille, J. C., Hall, W. D., Nardi, B., Massie, S., Yudin, V., Khosravi, R., Konopka, P., and Tarasick, D.: Tropospheric intrusions associated with the secondary tropopause, J. Geophys. Res., 114, D10302, https://doi.org/10.1029/2008JD011374, 2009.

Ploeger, F. and Birner, T.: Seasonal and inter-annual variability of lower stratospheric age of air spectra, Atmos. Chem. Phys., 16, 10195–10213, https://doi.org/10.5194/acp-16-10195-2016, 2016.

Ploeger, F., Legras, B., Charlesworth, E., Yan, X., Diallo, M., Konopka, P., Birner, T., Tao, M., Engel, A., and Riese, M.: How robust are stratospheric age of air trends from different reanalyses?, Atmos. Chem. Phys., 19, 6085–6105, https://doi.org/10.5194/acp-19-6085-2019, 2019.

Podglajen, A. and Ploeger, F.: Retrieving the age of air spectrum from tracers: principle and method, Atmos. Chem. Phys., 19, 1767–1783, https://doi.org/10.5194/acp-19-1767-2019, 2019.

Ray, E.: SEAC4RS UTLS transport data set, [data set], available at https://csl.noaa.gov/groups/csl8/modeldata (last access: 24 September, 2021), 2021a.

Ray, E.: SEAC4RS UTLS transport study IDL code, [code], available at https://csl.noaa.gov/groups/csl8/modeldata (last access: 30 April, 2022), 2021b.

Ray, E. A., Moore, F. L., Elkins, J. W., Dutton, G. S., Fahey, D. W., Vomel, H., Oltmans, S. J., and Rosenlof, K. H.: Transport into the Northern Hemisphere lowermost stratosphere revealed by in situ tracer measurements, J. Geophys. Res., 104, 26565–26580, 1999.

Ray, E. A., Rosenlof, K. H., Richard, E. C., Hudson, P. K., Cziczo, D. J., Loewenstein, M., Jost, H.-J., Lopez, J., Ridley, B., Weinheimer, A., Montzka, D., Knapp, D., Wofsy, S. C., Daube, B. C., Gerbig, C., Xueref, I., and Herman, R. L.: Evidence of the effect of summertime midlatitude convection on the subtropical lower stratosphere from CRYSTAL-FACE tracer measurements, J. Geophys. Res., 109, D18304, https://doi.org/10.1029/2004JD004655, 2004.

Saltzman, E. S., Aydin, M., De Bruyn, W. J., King, D. B., and Yvon-Lewis, S. A.: Methyl bromide in preindustrial air: Measurements from and Antarctic ice core, J. Geophys. Res., 109, D05301, https://doi.org/10.1029/2003JD004157, 2004.

Schoeberl, M. R., Sparling, L. C., Jackman, C. H., and Fleming, E. L.: A Lagrangian vew of stratospheric trace gas distributions, J. Geophys. Res., 105, 1537–1552, 2000.

Singh, H. B., Thakur, A. N., Chen, Y. E., and Kanakidou, M.: Tetrachloroethylene as an indicator of low Cl atom concentrations in the atmosphere, Geophys. Res. Lett., 23, 1529–1532, 1996.

Tang, J.-H., Chan, L.-Y., Chan, C.-Y., Li, Y.-S., Chang, C.-C., Liu, S.-C., and Li, Y.-D.: Nonmethane hydrocarbons in the transported and local air masses at a clean remote site on Hainan Island, south China, J. Geophys. Res., 112, D14316, https://doi.org/10.1029/2006JD024297, 2007.

Toon, O. B., Maring, H., Dibb, J., Ferrare, R., Jacob, D. J., Jensen, E. J., Luo, Z. J., Mace, G. G., Pan, L. L., Pfister, L., Rosenlof, K. H., Redemann, J., Reid, J. S., Singh, H. B., Thompson, A. M., Yokelson, R., Minnis, P., Chen, G., Jucks, K. W., and Pszenny, A.: Planning, implementation, and scientific goals of the Studies of Emissions and Atmospheric Composition, Clouds and Climate Coupling by Regional Surveys (SEAC^{4}RS) field mission, J. Geophys. Res., 121, 4967–5009, https://doi.org/10.1002/2015JD024297, 2016.

von Hobe, M., Ploeger, F., Konopka, P., Kloss, C., Ulanowski, A., Yushkov, V., Ravegnani, F., Volk, C. M., Pan, L. L., Honomichl, S. B., Tilmes, S., Kinnison, D. E., Garcia, R. R., and Wright, J. S.: Upward transport into and within the Asian monsoon anticyclone as inferred from StratoClim trace gas observations, Atmos. Chem. Phys., 21, 1267–1285, https://doi.org/10.5194/acp-21-1267-2021, 2021.

Waugh, D. W. and Hall, T. M.: Age of stratospheric air: Theory, observations, and models, Rev. Geophys., 40, 1010, https://doi.org/10.1029/2000RG00101, 2002.

Waugh, D. W., Crotwell, A. M., Dlugokencky, E. J., Dutton, G. S., Elkins, J. W., Hall, B. D., Hintsa, E. J., Hurst, D. F., Montzka, S. A., Mondeel, D. J., Moore, F. L., Nance, J. D., Ray, E. A., Steenrod, S. D., Strahan, S. E., and Sweeney, C.: Tropospheric SF$_6$: Age of air from the Northern Hemisphere midlatitude surface, J. Geophys. Res., 118, 11429–11441, https://doi.org/10.1002/jgrd.50848, 2013.

Weinstock, E. M., Pittman, J. V., Sayres, D. S., Smith, J. B., Anderson, J. G., Wofsy, S. C., Xueref, I., Gerbig, C., Daube, B. C., Pfister, L., Richard, E. C., Ridley, B. A., Weinheimer, A. J., Jost, H.-J., Lopez, J. P., Loewenstein, M., and Thompson, T. L.: Quantifying the impact of the North American monsoon and deep midlatitude convection on the subtropical lowermost stratosphere using in situ measurements, J. Geophys. Res., 112, D18310, https://doi.org/10.1029/2007JD008554, 2007.

WMO (World Meteorological Organization): Scientific Assessment of Ozone Depletion: 2018, Global Ozone Research and Monitoring Project-Report No. 58, 588 pp., Geneva, Switzerland, 2018.

Wuebbles, D. J., Patten, K. O., Wang, D., Youn, D., Martínez-Avilés, M., and Francisco, J. S.: Three-dimensional model evaluation of the Ozone Depletion Potentials for n-propyl bromide, trichloroethylene and perchloroethylene, Atmos. Chem. Phys., 11, 2371–2380, https://doi.org/10.5194/acp-11-2371-2011, 2011.

Yan, X., Konopka, P., Hauck, M., Podglajen, A., and Ploeger, F.: Asymmetry and pathways of inter-hemispheric transport in the upper troposphere and lower stratosphere, Atmos. Chem. Phys., 21, 6627–6645, https://doi.org/10.5194/acp-21-6627-2021, 2021.

Yu, P., Rosenlof, K. H., Lui, S., Telg, H., Thornberry, T. D., Rollins, A. W., Portmann, R. W., Bai, Z., Ray, E. A., Duan, Y., Pan, L. L., Toon, O. B., Bian, J., and Gao, R.-S.: Efficient transport of tropospheric aerosol into the stratosphere via the Asian summer monsoon anticyclone, P. Natl. Acad. Sci. USA, 114, 6972–6977, https://doi.org/10.1073/pnas.1701170114, 2017.